JEM Journal of Experimental Medicine

ARTICLE

Locus folding mechanisms determine modes of antigen receptor gene assembly

Brittney M. Allyn[1,2], Katharina E. Hayer[2,3,4], Clement Oyeniran[5], Vincent Nganga[5], Kyutae Lee[2], Bikash Mishra[5], Ahmet Sacan[3], Eugene M. Oltz[5], and Craig H. Bassing[1,2]

The dynamic folding of genomes regulates numerous biological processes, including antigen receptor (AgR) gene assembly. We show that, unlike other AgR loci, homotypic chromatin interactions and bidirectional chromosome looping both contribute to structuring *Tcrb* for efficient long-range V(D)J recombination. Inactivation of the CTCF binding element (CBE) or promoter at the most 5′Vβ segment (*Trbv1*) impaired loop extrusion originating locally and extending to DβJβ CBEs at the opposite end of *Tcrb*. Promoter or CBE mutation nearly eliminated *Trbv1* contacts and decreased RAG endonuclease-mediated *Trbv1* recombination. Importantly, *Trbv1* rearrangement can proceed independent of substrate orientation, ruling out scanning by DβJβ-bound RAG as the sole mechanism of Vβ recombination, distinguishing it from *Igh*. Our data indicate that CBE-dependent generation of loops cooperates with promoter-mediated activation of chromatin to juxtapose Vβ and DβJβ segments for recombination through diffusion-based synapsis. Thus, the mechanisms that fold a genomic region can influence molecular processes occurring in that space, which may include recombination, repair, and transcriptional programming.

Introduction

The dynamic organization of three-dimensional genome structure regulates important aspects of DNA transcription, replication, recombination, and repair, and is controlled by two fundamental mechanisms in interphase cells. Interactions among chromatin regions of similar transcriptional activity and covalent histone modifications, referred to as homotypic chromatin interactions, contribute to genome-wide architecture in all eukaryotes (Eagen, 2018; Hildebrand and Dekker, 2020; Luppino and Joyce, 2020; Penagos-Puig and Furlan-Magaril, 2020; Rowley and Corces, 2018). These homotypic interactions are mediated by multiple mechanisms, which include coalescence of heterochromatin binding proteins or transcription factors via phase separation, homotypic contacts between transcriptionally active or repressive histone marks, and promoter–promoter or promoter–enhancer contacts in microenvironments known as transcription factories (Boija et al., 2018; Chong et al., 2018; Csink and Henikoff, 1996; Falk et al., 2019; Ganai et al., 2014; Gotzmann and Foisner, 1999; Harrison et al., 2021; Hilbert et al., 2021; Li et al., 2012; Rowley et al., 2017; Wang et al., 2019). In higher-order eukaryotes, point-to-point contacts that fold chromosomes are mediated by active extrusion of DNA to form loops that are anchored by DNA-binding proteins (Dixon et al., 2012; Rao et al., 2014). Loop extrusion relies on the cohesin complex, which loads onto chromosomes mainly at enhancers and promoters (Kagey et al., 2010), then translocates back and forth along DNA until its movement in one direction is halted by an occupied CTCF binding element (CBE). The blocked cohesin spools DNA from the other direction until reaching another bound CBE, generating a transient loop (Davidson et al., 2019; Fudenberg et al., 2016; Kim et al., 2019; Sanborn et al., 2015). As CBEs have asymmetrical sequences, and the CTCF N-terminus binds cohesin (Li et al., 2020), the effectiveness of CBEs for impeding cohesin depends on their linear genomic orientations, with CBEs of convergent orientation providing more durable loop anchors than CBEs in the same orientation (de Wit et al., 2015; Rao et al., 2014). Additional impediments to cohesin can anchor loops, including active transcription and chromatin-bound proteins other than CTCF (Busslinger et al., 2017; Jeppsson et al., 2022; Wutz et al., 2017; Zhang et al., 2019). Homotypic chromatin interactions and chromosome looping each also orchestrate functional interactions between cis-acting DNA elements, most commonly transcriptional promoters and enhancers (Dowen et al., 2014;

[1]Immunology Graduate Group, Perelman School of Medicine, University of Pennsylvania, Philadelphia, PA, USA; [2]Department of Pathology and Laboratory Medicine, Children's Hospital of Philadelphia, Perelman School of Medicine, University of Pennsylvania, Philadelphia, PA, USA; [3]Biomedical Engineering Doctoral Degree Program, School of Biomedical Engineering, Science and Health Systems, Drexel University, Philadelphia, PA, USA; [4]Department of Biomedical and Health Informatics, Children's Hospital of Philadelphia, Perelman School of Medicine, Philadelphia, PA, USA; [5]Department of Microbial Infection and Immunity, Ohio State College of Medicine, Ohio State University, Columbus, OH, USA.

Correspondence to Craig H. Bassing: bassing@email.chop.edu; Eugene M. Oltz: eugene.oltz@osumc.edu.

Flavahan et al., 2016; Hnisz et al., 2016; Ji et al., 2016; Lupiáñez et al., 2015; Narendra et al., 2015). Importantly, the precise molecular mechanisms and functional relationships between these two fundamental means of genome folding and how they regulate biological processes remain matters of broad interest.

A particularly relevant example of the interplay between genome architecture and function is the diversification of antigen receptor (AgR) genes through the process of V(D)J recombination, which is the molecular basis for adaptive immunity in jawed vertebrates. Precursor B and T cells employ lineage- and developmental stage–specific mechanisms that facilitate physical interactions between recombining gene segments separated by up to 3 Mb (Allyn et al., 2020; Carico and Krangel, 2015; Ribeiro de Almeida et al., 2015; Ebert et al., 2015; Jhunjhunwala et al., 2008; Kenter and Feeney, 2019; Proudhon et al., 2015; Zhang et al., 2022). The lymphocyte-specific, heterotetrametric $RAG1_2/RAG2_2$ (RAG) endonuclease mediates recombination between variable (V), diversity (D), and joining (J) gene segments within a given AgR locus. The RAG complex initially binds a recombination signal sequence (RSS) flanking one gene segment, captures a compatible RSS of a different segment (synapsis), and then cleaves DNA at each segment/RSS junction (Bassing et al., 2002; Schatz and Swanson, 2011). The four liberated DNA ends are repaired by non-homologous end-joining proteins, generating a precise RSS–RSS signal join and a processed V(D)J coding join (Bassing et al., 2002; Schatz and Swanson, 2011). The assembled V(D)J gene segments and downstream constant region exons comprise a complete AgR gene. Notably, RAG-mediated recombination can proceed through deletion or inversion of intervening sequences depending on whether the participating RSSs reside in convergent or identical linear genomic orientation, respectively.

V(D)J recombination is regulated at numerous levels with cell type, developmental stage, and allele specificity. At endogenous AgR loci, RAG targeting is facilitated by the sequential activation of transcriptional enhancers and gene segment-proximal promoters, which render RSSs accessible (Barajas-Mora et al., 2023; Bhat et al., 2023; Krangel, 2003; Majumder et al., 2015a; Sakamoto et al., 2012; Schlissel, 2004; Sleckman et al., 1996). In developing B and T cells, RAG is initially allowed access to DJ segments at *Igh* and *Tcrb*, respectively, forming recombination centers (RCs) that mediate short-range D-to-J recombination (Ji et al., 2010b). RAG-bound DJ complexes must then capture a V RSS to conduct V-to-DJ rearrangement. In the later stages of B and T cell development, RAG establishes RCs over *Igk* and *Tcra* J segments, respectively, to capture a V RSS for V-to-J recombination (Ji et al., 2010b). The importance of efficiently targeting and completing V(D)J recombination is evidenced by mutations that attenuate RAG endonuclease activity and AgR gene assembly, which cause immunodeficiencies characterized by limited numbers of mature lymphocytes and restricted AgR diversity (Delmonte et al., 2018).

The germline configurations of AgR loci pose a common challenge for their efficient assembly, since V and (D)J segments, separated by up to 3 Mb, must be brought into close spatial proximity for RSS capture. In the absence of locus folding, long-range V-to-(D)J synapsis through diffusion-based collision is highly unlikely and would lead to extremely biased usage of RC-proximal V segments. Indeed, the *Igh*, *Igk*, *Tcrb*, and *Tcra/d* loci each undergo lineage- and developmental stage–specific contraction to bring V segments into close spatial proximity with their (D)J segments (Fuxa et al., 2004; Jhunjhunwala et al., 2008; Kosak et al., 2002; Roldán et al., 2005; Shih and Krangel, 2010; Skok et al., 2007). Long-range contacts within AgR loci are likely mediated by CBEs that are interspersed among the V segments and oriented convergently with CBEs flanking their respective RCs (Loguercio et al., 2018). Indeed, cohesin and/or CTCF-dependent contacts between convergent V and RC CBEs enhance long-range V-to-(D)J recombination at these four loci (Hill et al., 2023; Seitan et al., 2011; Shih et al., 2012; Majumder et al., 2015b; Zhang et al., 2019). In addition, homotypic interactions between transcriptionally active V and (D)J chromatin have been proposed to fold AgR loci and stimulate V-to-(D)J recombination by facilitating diffusion-based synapsis (Verma-Gaur et al., 2012).

The mechanisms that generate AgR architectures also contribute to which RSSs are allowed to synapse for RAG-mediated recombination. Theoretically, locus compaction through cohesin/CBE-mediated chromosome looping or homotypic chromatin interactions could promote synapsis of RSSs via diffusion-based collisions independent of their genomic orientations, thereby permitting deletional or inversional recombination (Bassing et al., 2008; Jhunjhunwala et al., 2008; Ji et al., 2010b; Ranganath et al., 2008; Wu et al., 2003, 2007). However, next-generation sequencing (NGS) of RAG-mediated rearrangements in the mouse *Igh* and *Tcra/d* loci revealed nearly exclusive participation of bona fide or cryptic RSSs in convergent genomic orientation, resulting in only deletional V-to-(D)J rearrangements (Dai et al., 2021; Hill et al., 2020; Zhao et al., 2016). The observed restriction in RSS orientation at these loci led to a mechanistic model wherein cohesin-driven chromosome loop extrusion originates from a RAG-bound RSS and progressively spools DNA past this obstacle, enabling the open RAG active site to linearly and unidirectionally scan loci for capture of a convergent RSS (Ba et al., 2020; Dai et al., 2021; Hill et al., 2020; Jain et al., 2018; Zhang et al., 2019). In support of this RAG scanning model for synapsis, *Igh* folding in RAG-deficient pro-B cells proceeds predominantly by loop extrusion anchored at the D_HJ_H end of the locus that spools through upstream V_H segments (Hill et al., 2023). Although it remains possible that RAG scanning from RCs is a primary mechanism for long-range V-to-(D)J recombination at all AgR loci, it cannot conduct rearrangements that proceed through inversion between RSSs with identical linear genomic orientations in *Igk* and *Tcrb* loci (Ribeiro de Almeida et al., 2015; Lee and Bassing, 2020; Wu et al., 2020). These inversional *Igk* and *Tcrb* rearrangements must depend on topological changes that place V and (D)J RSSs in spatial proximity to facilitate synapsis through random diffusion-based collisions.

We now show that *Tcrb* loci adopt intralocus contacts formed via a combination of homotypic chromatin interactions and bidirectional chromosome loop extrusion between Vβ gene segments and the DβJβ RC in double-negative ($CD4^-CD8^-$, DN)

thymocytes poised to undergo recombination. To determine the independent contributions of homotypic interactions and looping in these processes, we focused on the most RC-distal Vβ gene segment (*Trbv1*) and its single proximal CBE. Because *Trbv1* is isolated from all other *Tcrb* gene segments and CBEs by 150 kb, we could cleanly dissect the impact of promoter-driven compartmentalization and CBE-mediated looping on locus folding and recombination, independent of neighboring transcriptional and architectural cis elements. Indeed, mutation of its proximal CBE had no significant impact on local chromatin but dramatically diminished loop extrusion initiating from the *Trbv1* region, nearly eliminating *Trbv1-RC* loops, contacts, and recombination. Likewise, promoter deletion profoundly impaired loop extrusion emanating from *Trbv1*, as well as *Trbv1*-RC loops, contacts, and recombination, despite retaining CTCF occupancy over the *Trbv1* CBE. Moreover, unlike at *Igh*, an RSS engineered to have a flipped linear genomic orientation mediates inversional *Trbv1* rearrangements with DβJβ segments, which cannot occur by a RAG scanning mechanism. Therefore, we conclude that Vβ CBE-dependent loop extrusion and resultant chromosome loops, in addition to promoter-driven homotypic chromatin interactions, fold activated *Tcrb* loci for recombination in DN thymocytes. These cooperative architectural mechanisms augment physical interactions between Vβ and DβJβ segments, facilitating their recombination via diffusion-based synapsis. Our findings have broad implications for how the mechanisms of genome folding interface to regulate other biological processes.

Results

Tcrb architecture in DN thymocytes

As a prelude to mechanistic studies, we generated a map of DNA contacts for *Tcrb* loci that were poised to undergo V(D)J recombination. For this purpose, we performed HiC analyses on DN thymocytes from RAG-deficient mice, in which *Tcrb* gene segments are transcriptionally active but cannot rearrange due to the lack of active recombinase complexes. The most salient features of the *Tcrb* locus, which spans 670 kb on mouse chromosome 6, are shown in Fig. 1 A (Majumder et al., 2015a). In brief, the most 5′Vβ segment, *Trbv1*, resides 150 kb upstream of the main Vβ cluster (*Trbv2* through *Trbv30*; 250 kb), with all these Vβ segments configured to rearrange by deletion. In turn, this Vβ cluster lies 250 kb upstream of two Dβ-Jβ-Cβ clusters (Dβ1-Jβ1-Cβ1, Dβ2-Jβ2-Cβ2) and, at the 3′ terminus of the locus, a lone Vβ segment (*Trbv31*) in an orientation that restricts it to inversional recombination (Fig. 1 A; Majumder et al., 2015a). Regions on either side of the main Vβ cluster contain multiple trypsinogen genes, none of which are expressed in T lineage cells (Majumder et al., 2015a). Transcription within *Tcrb* is controlled by a single known enhancer (Eβ), which is positioned between the second Dβ-Jβ-Cβ cluster and *Trbv31*, as well as promoters that lie upstream of each Vβ and Dβ segment (Gopalakrishnan et al., 2013; Mathieu et al., 2000; McMillan and Sikes, 2008; Sikes et al., 2002; Whitehurst et al., 1999). The Dβ promoters and Eβ are required for RAG to access DβJβ segments and for the formation of two independent RCs (Ji et al., 2010a). *Tcrb* architectural elements include 18 CBEs interspersed among its Vβ segments, all of which are oriented convergently relative to three CBEs flanking the DβJβ segments: 5′PC and CBE1 (27 and 3 kb upstream of Dβ1, respectively) and CBE3 (between Eβ and *Trbv31*; Fig. 1 A; Loguercio et al., 2018; Majumder et al., 2015b). For simplicity, we refer to *Tcrb* sequences from 5′PC through CBE3 as the RC region.

To elucidate topological mechanisms that fold *Tcrb* loci, we complemented HiC analyses for DNA contacts with RNA sequencing (RNA-Seq) and chromatin immunoprecipitation sequencing (ChIP-Seq) to characterize transcriptional and chromatin activities. Our use of RAG-deficient (*Rag1*$^{-/-}$) DN thymocytes eliminated complications that arise from the multitude of *Tcrb* configurations present in actively recombining thymocytes. A heatmap for DNA contacts was generated from six independent HiC experiments, each performed on thymocytes pooled from at least five mice (Fig. 1 B and Table S1). Because HiC is a population-based analysis, these data presumably reflect a range of *Tcrb* architectures present in DN thymocytes but reveal several prominent patterns of interactions (Fig. 1 B). First, the main Vβ cluster partitions into a distinct topological domain that interacts more with itself than sequences of flanking domains (Fig. 1 B). This feature may reflect homotypic chromatin interactions since all functional Vβ segments within the main cluster are transcribed and enriched for H3K27ac (active chromatin), whereas its flanking domains lack transcripts and are decorated by H3K9me2 (inactive chromatin; Fig. 1 C). Second, the Vβ cluster exhibits robust contacts with the RC region, which harbors highly transcribed DβJβ segments and chromatin enriched for H3K27ac, while sharply segregating from upstream inactive chromatin spanning silent trypsinogen genes (Fig. 1, B and C). The *Trbv12.2* and *Trbv13.2* Vβ segments have the most intense contacts with RC chromatin, which correlates with their very high levels of germline transcripts and H3K27ac (Fig. 1, B and C). Third, the isolated and transcriptionally active *Trbv1* segment makes a trail of contacts through active chromatin over the main Vβ cluster and the RC, but interacts infrequently with intervening regions of silent chromatin, together forming a segmented stripe originating at *Trbv1* (Fig. 1, B and C). These findings are consistent with a role for homotypic chromatin interactions mediated by alternating active and inactive chromatin domains, which folds *Tcrb* to position all Vβ, Dβ, and Jβ gene segments near each other, but spatially segregate them from silent regions.

To identify anchored loops in *Tcrb*, we analyzed the HiC data from DN thymocytes with the MUSTACHE algorithm. As shown in Fig. 1, B and C, nearly all of the loop anchors map near (i) CBEs occupied by CTCF and the cohesin subunit RAD21, (ii) transcriptionally active gene segments, or (iii) both (Fig. 1, B and C). Most loops form between Vβ regions with CBEs that have the same linear genomic orientation or between Vβ and RC CBEs that are in a convergent orientation (Fig. 1, B and C). This range of anchoring is exemplified by *Trbv1*, whose CBE forms loops with a CBE of the same orientation located between *Trbv3* and *Trbv4*, with a region between *Trbv10* and *Trbv11*, and with two of the convergent CBEs, 5′PC, and CBE3, which flank the RC (Fig. 1, B and C). Similarly, the CBE between *Trbv3* and *Trbv4* loops with

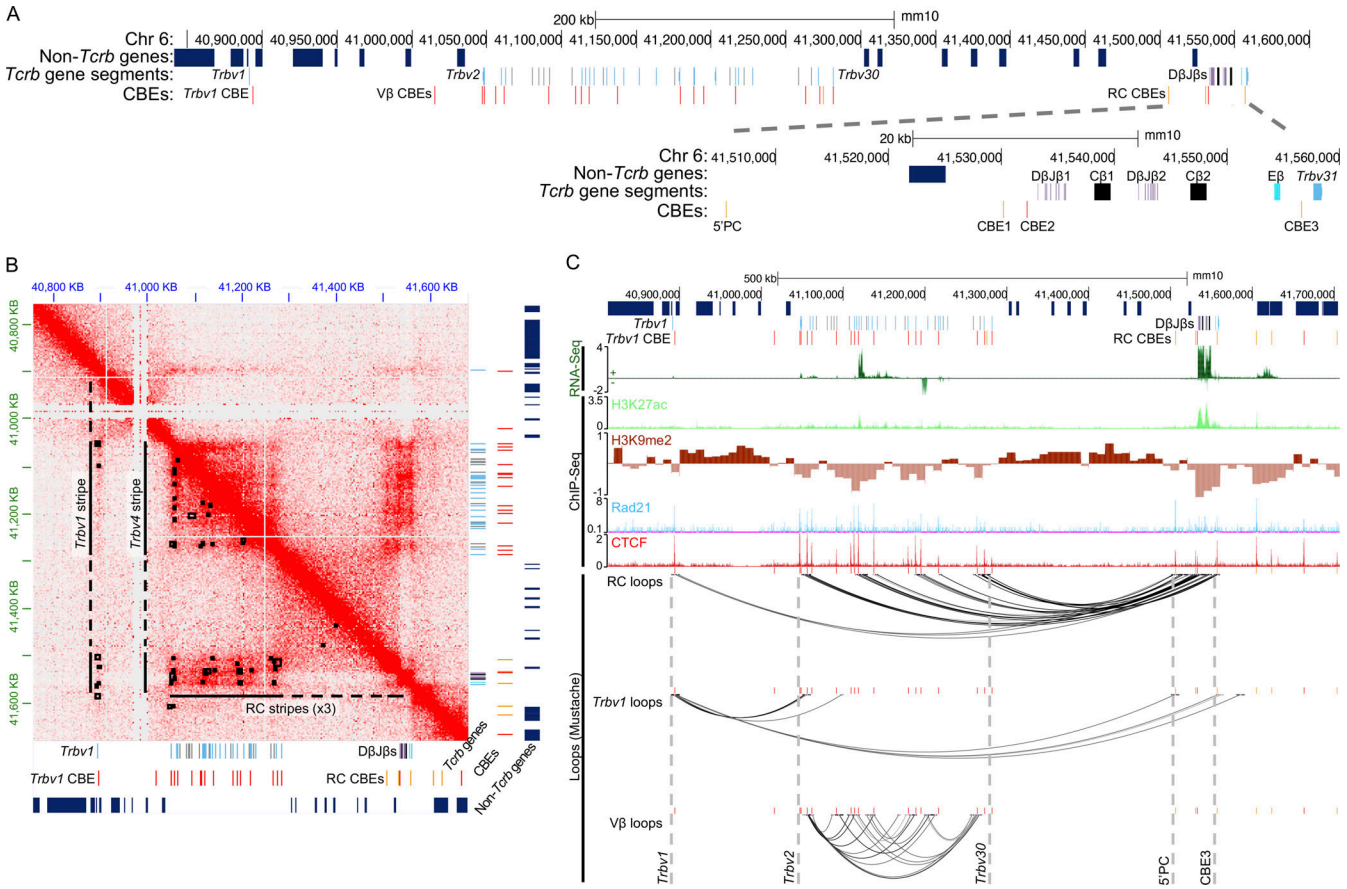

Figure 1. **Homotypic chromatin interactions and chromosome looping fold *Tcrb* loci in thymocytes. (A)** Schematic view of mouse chromosome 6 region spanning *Tcrb* with tracks presenting nucleotide position, non-*Tcrb* genes, *Tcrb* gene segments (functional or non-functional Vβ segments, light blue or black, respectively; Dβ segments, lavender; Jβ segments, purple; Cβ exons, black; Eβ, cyan) and CBEs (red for sense orientation or orange for antisense orientation). **(B)** HiC heat map of WT *Tcrb* loci in *Rag1*$^{-/-}$ mouse thymocytes. Data are combined from six independent experiments, each performed on cells pooled from at least five mice of either sex and presented at 3 kb resolution. The lower panel indicates loops (black squares) identified by MUSTACHE performed at 3, 5, or 10 kb resolution, and segmented stripes (lines). **(C)** Genome browser views depicting two replicates each of RNA-Seq (sense and antisense transcripts) or a representative of two replicates of ChIP-Seq for H3K27ac, H3K9me2, Rad21 (GSM2973690), or CTCF for WT *Tcrb* of *Rag1*$^{-/-}$ thymocytes. Below are MUSTACHE loops from panel B now filtered and separated by interactome. The top track shows loops with at least one anchor within the RC (between 5′PC and CBE3). The middle track shows loops with one anchor at *Trbv1*. The bottom track shows loops with both anchors in the main Vβ cluster. RNA-Seq and ChIP-Seq data are shown as reads per million, except for H3K9me2, which is shown as the $\log_2$ ratio of bound H3K9me2 over input control (enriched for = dark brown above axis; depletion of = light brown below axis).

CBEs of the same orientation lying near a number of Vβ gene segments (*Trbv11*, *Trbv12.1*, *Trbv14*, *Trbv20*, or *Trbv28*), with regions lacking CBEs near *Trbv17* or *Trbv22*, and with all three convergent CBEs flanking the RC (Fig. 1, B and C).

Stripes of contacts emanating from the axis of HiC heatmaps from a cellular population provide information about the direction(s) of loop extrusion across a genetic locus. These architectural features are considered to represent asymmetrical loop extrusion, wherein sequences on the axis are the stationary anchor for loop extrusion, and the stripe results from cells captured at different points along the trajectory of the loop extrusion event (Barrington et al., 2019; Fudenberg et al., 2016; Mirny et al., 2019; Vian et al., 2018). In addition to the segmented stripe originating near *Trbv1*, striking features emerging from these HiC data include similar segmented stripes emanating from either Vβ or RC regions (Fig. 1 B). As with *Trbv1*, stripes anchored at *Trvb4* or RC CBEs interact more with Vβ gene segments than with intervening silent trypsinogen genes (Fig. 1 B). The presence of these segmented stripes is consistent with cohesin-driven loop extrusion anchored at Vβ or RC CBEs and progressing downstream or upstream, respectively. We envision that this bidirectional loop extrusion is dispersed across cells whereby loop extrusion proceeds from a Vβ CBE to an RC CBE in some cells and from an RC CBE to a Vβ CBE in other cells. The HiC maps indicate that such loop extrusion is impeded more frequently when crossing chromatin stretches that are transcriptionally active and enriched for CTCF, leading to a higher frequency of captured contacts. In contrast, regions that are transcriptionally repressed and depleted for CTCF, particularly the spans of silent trypsinogen genes, likely pose little impediment to loop extrusion, leading to a paucity of captured contacts with the anchor. Together, HiC data support roles for both homotypic chromatin interactions and chromosome looping as cooperative mechanisms that fold *Tcrb* loci, positioning the

collection of Vβ segments into spatial proximity with the two RCs to mediate efficient recombination across large genomic distances and normalized distribution of Vβ segments.

The *Trbv1* CBE and promoter are determinants of *Tcrb* recombination and architecture

To independently assess functions of chromosome looping and homotypic chromatin interactions in long-range Vβ-to-DβJβ recombination, we focused on *Trbv1* for several reasons, including (i) it is the most RC-distal Vβ segment, (ii) it has a downstream CBE and its own promoter, (iii) it is 150 kb away from the remaining cluster of Vβ cluster segments, allowing us to test regulatory elements without influence from neighboring counterparts, (iv) a distinct contact stripe, indicative of loop extrusion, emanates from this region, and (v) *Trbv1* is flanked on both sides by transcriptionally inactive, CTCF-depleted chromatin in DN thymocytes. Accordingly, we took a genetic approach, using CRISPR/Cas9-mediated genomic editing to either replace the *Trbv1* CBE with a scramble sequence (Jain et al., 2018) or to delete a 1,245 bp region that contains the *Trbv1* promoter (Fig. 2 A; Gopalakrishnan et al., 2013). We reasoned that the CBE mutation would abolish CTCF binding without altering *Trbv1* transcriptional activity, allowing us to determine whether it loops with convergent RC CBEs by anchoring and/or terminating loop extrusion. Conversely, mutation of the *Trbv1* promoter would abrogate transcription and chromatin activation, potentially without reducing CTCF occupancy, enabling us to assess whether the promoter orchestrates homotypic chromatin interactions. Notably, we also expected that *Trbv1* promoter inactivation would render the *Trbv1* RSS inaccessible to RAG, thereby preventing *Trbv1* recombination independent of promoter functions in folding *Tcrb*.

We first established RAG-sufficient mice with homozygous inactivation of the *Trbv1* CBE ($V1C^{Scr/Scr}$ mice) or promoter ($V1P^{KO/KO}$ mice) to determine whether these cis elements shape TCRβ repertoires by stimulating long-range *Trbv1*-to-DβJβ rearrangements. As revealed by flow cytometry, the fraction of thymic αβ T cells with surface expression of TRBV1 was dramatically reduced in each mutant strain (Fig. 2 B). Specifically, TRBV1 was displayed on 5.3% of wild-type (*WT*) cells, 1.5% of $V1C^{Scr/Scr}$ cells (a 3.5-fold decrease), and 0.13% of $V1P^{KO/KO}$ cells (a 40.8-fold decrease; Fig. 2, B and C). To directly ascertain the effects of each mutation on *Trbv1* recombination in DNA from unselected DN thymocytes, we used Adaptive Immunosequencing, a commercial NGS platform. In WT cells, 4.4% of unique Vβ-to-DβJβ rearrangements (in-frame and out-of-frame combined) involved *Trbv1*, compared with 0.8% in $V1C^{Scr/Scr}$ cells [a 6-fold decrease] and 0.1% in $V1P^{KO/KO}$ cells (a 48-fold decrease; Fig. 2 D and Table S2). Notably, residual *Trbv1* recombination in both mutants retained a normal distribution of coding joins to Dβ1Jβ1 versus Dβ2Jβ2 clusters (Fig. 2 E), precluding a bias for shorter-range events resulting from secondary Vβ rearrangements to the latter cluster. Collectively, our flow cytometry and sequencing data demonstrate that the *Trbv1* CBE and promoter are important determinants of *Trbv1*-to-DβJβ recombination in DN thymocytes, cooperating to ensure robust representation of TRBV1 within the TCRβ repertoire.

The *Trbv1* CBE stimulates recombination by anchoring and terminating loop extrusion

To investigate underlying mechanisms for CBE-mediated recombination of *Trbv1*, we bred $V1C^{Scr/Scr}$ mice onto a $Rag1^{-/-}$ background and profiled *Tcrb* contacts and chromatin in DN thymocytes. For each *Trbv1* mutant, we conducted HiC on two, independent DN samples and combined data (Fig. 3 A and Table S1). The HiC data from WT and mutant samples were downsampled to reflect an identical number of reads. As compared with *WT* cells, $V1C^{Scr/Scr}$ thymocytes had a striking reduction of *Trbv1* contacts with other downstream *Tcrb* elements (Fig. 3, A and B). The prominent segmented stripe emanating from *Trbv1* was significantly attenuated in the mutant thymocytes, including its progression through the main Vβ cluster and RC regions (Fig. 3, A and B). Consistent with this observation, MUSTACHE failed to identify loops between the inactivated *Trbv1* CBE and other *Tcrb* elements in $V1C^{Scr/Scr}$ cells (Fig. 3, A and C). Notably, while very low-level contacts between *Trbv1* and sequences spanning other Vβ segments or the RC were detectable in $V1C^{Scr/Scr}$ thymocytes, interactions between the mutant *Trbv1* CBE and convergent 5′*PC* CBE, which still binds CTCF, were absent (Fig. 3 B). As anticipated, the mutant *Trbv1* CBE lacked CTCF occupancy but retained transcriptional activity and H3K27ac levels at *Trbv1* (Fig. 3 D). However, we detected a modest extension of H3K9me2 and reductions of H3K7ac and transcripts on $V1C^{Scr}$ alleles relative to WT alleles (Fig. 3, C and D). These modest changes in chromatin could reflect, respectively, (i) loop extrusion events initiating from the RC that now extend past the inactivated CBE and pull *Trbv1* away from the nuclear lamina and (ii) reduced *Trbv1* contacts with the RC, which may diminish cooperative effects of homotypic interactions on reinforcing active chromatin modifications. It is possible that the slightly lower activity of *Trbv1* chromatin in $V1C^{Scr/Scr}$ thymocytes contributes to reduced *Trbv1* recombination. Nevertheless, these results indicate that the *Trbv1* CBE functions as a primary anchor for loop extrusion that originates from the *Trbv1* region, generating contacts/loops with downstream *Tcrb* sequences (*Trbv1* stripe), including the RC, and promoting *Trbv1* recombination. In addition to this function, our data are consistent with the *Trbv1* CBE acting as a terminal anchor for loop extrusion that originates from RC regions, forming loops between the RC and *Trbv1* that drive its rearrangement. The low levels of *Trbv1* contacts and rearrangements with the RC in $V1C^{Scr/Scr}$ cells could still proceed through the *Trbv1* promoter, which may serve as a less efficient initiating or terminal anchor for loop extrusion compared with alleles that have the functional *Trbv1* CBE. We conclude that cohesin-mediated extrusion occurs in both directions across *Tcrb*, creating chromosome loops anchored at the *Trbv1* CBE to juxtapose *Trbv1* with DβJβ segments and stimulate their long-range recombination.

Promoter-mediated homotypic chromatin interactions drive *Trbv1* rearrangement

To elucidate how the promoter of *Trbv1* stimulates its long-range recombination, we profiled *Tcrb* contacts and chromatin in DN thymocytes from $V1P^{KO/KO}$ $Rag1^{-/-}$ mice. As compared with *WT* cells, $V1P^{KO/KO}$ thymocytes had a profound reduction in *Trbv1*

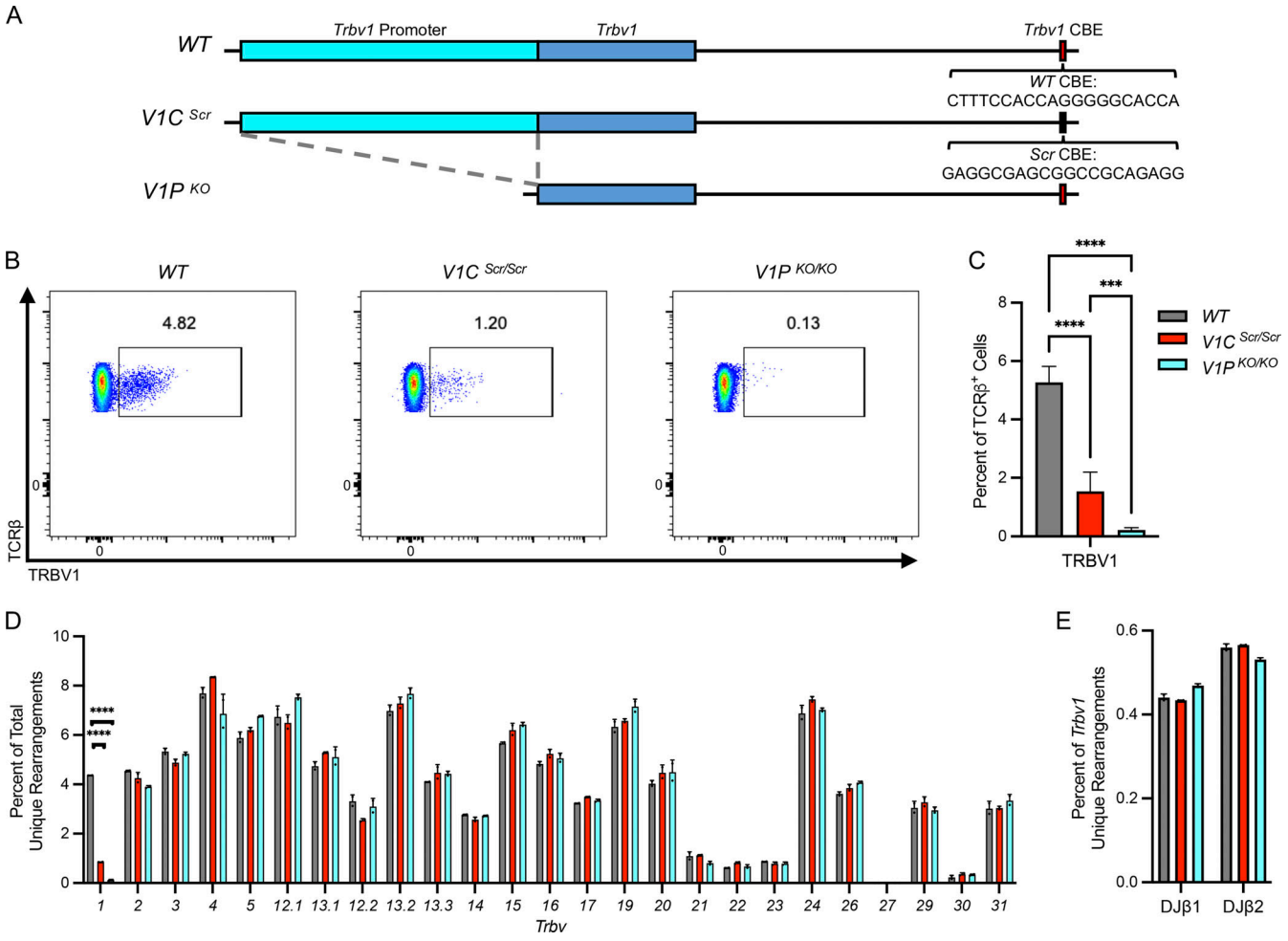

Figure 2. **The *Trbv1* CBE and promoter are determinants of *Tcrb* recombination and repertoire. (A)** Schematic representation of the *Trbv1* genomic region of the *WT*, CBE-inactivated (*V1C*^{Scr}), or promoter-deleted (*V1P*^{KO}) alleles. *WT* and scrambled CBE sequences are displayed. **(B)** Representative flow cytometry plots of thymic αβ T cells expressing TRBV1$^+$ TCRβ proteins on their surface in *WT*, *V1C*$^{Scr/Scr}$, or *V1P*$^{KO/KO}$ mice. Each plot displays the TRBV1$^+$TCRβ$^+$ gate and the percentage of total TCRβ$^+$ cells in the gate. **(C)** Quantification of TRBV1$^+$TCRβ$^+$ thymic αβ T cells in *WT* (n = 8), *V1C*$^{Scr/Scr}$ (n = 4), or *V1P*$^{KO/KO}$ (n = 7) mice. One-way ANOVA followed by Tukey's post-tests for multiple comparisons. ***P < 0.001 and ****P < 0.0001. **(D)** Quantification of the percentage of total unique *Tcrb* genes involving each Vβ gene segment from Adaptive Immunosequencing performed on DNA isolated from DN thymocytes of *WT*, *V1C*$^{Scr/Scr}$, or *V1P*$^{KO/KO}$ mice. n = 2, multiple unpaired t tests. ****, P < 0.0001. **(E)** Quantification of the percentage of *Trbv1* rearrangements to each of the two DβJβ clusters, calculated from data shown in panel D.

interactions with all other downstream *Tcrb* elements (Fig. 4, A and B). Indeed, we observed a nearly complete loss of the segmented stripe originating from *Trbv1*, as well as a complete loss of loops anchored near this gene segment (Fig. 4, A and C). As expected, *Trbv1* promoter deletion abrogated its transcription and dramatically reduced H3K27ac levels across *Trbv1* but had no significant impact on CTCF occupancy at the *Trbv1* CBE (Fig. 4 D). Our interpretation of these findings is that the promoter activates *Trbv1*, driving its homotypic interaction with transcriptionally active chromatin spanning the main Vβ and RC regions. Importantly, the promoter mutants lack a detectable loop between convergent *Trbv1* and 5′PC CBEs, despite CTCF occupancy at both sites (Fig. 4, C and D). This finding could be explained by several mechanisms that are not mutually exclusive, including (i) *Trbv1* promoter-mediated homotypic chromatin interactions stabilize contacts/loops formed with downstream *Tcrb* elements during loop extrusion from the *Trbv1* CBE, (ii) *Trbv1* promoter-mediated homotypic chromatin interactions function to stabilize *Trbv1*-RC loops created by cohesin-driven extrusion from the opposite direction, initially anchored at RC CBEs, and (iii) the *Trbv1* promoter serves as a loading site for cohesin complexes that mediate loop extrusion emanating from the *Trbv1* CBE. Collectively, these data support multifaceted roles for the *Trbv1* promoter in generating *Tcrb* architecture by contributing to homotypic chromatin interactions and cohesin-mediated loop extrusion emanating at both ends of the locus.

Orientation-independent RSS synapsis reveals a range of topological mechanisms for *Tcrb*

Our evidence supports a mechanistic model in which homotypic chromatin interactions and chromosome loop extrusion emanating from *Trbv1* cooperate to fold *Tcrb*. Importantly, neither mechanism is compatible with synapsis of RSSs solely by unidirectional RAG scanning from the RC, which requires loop

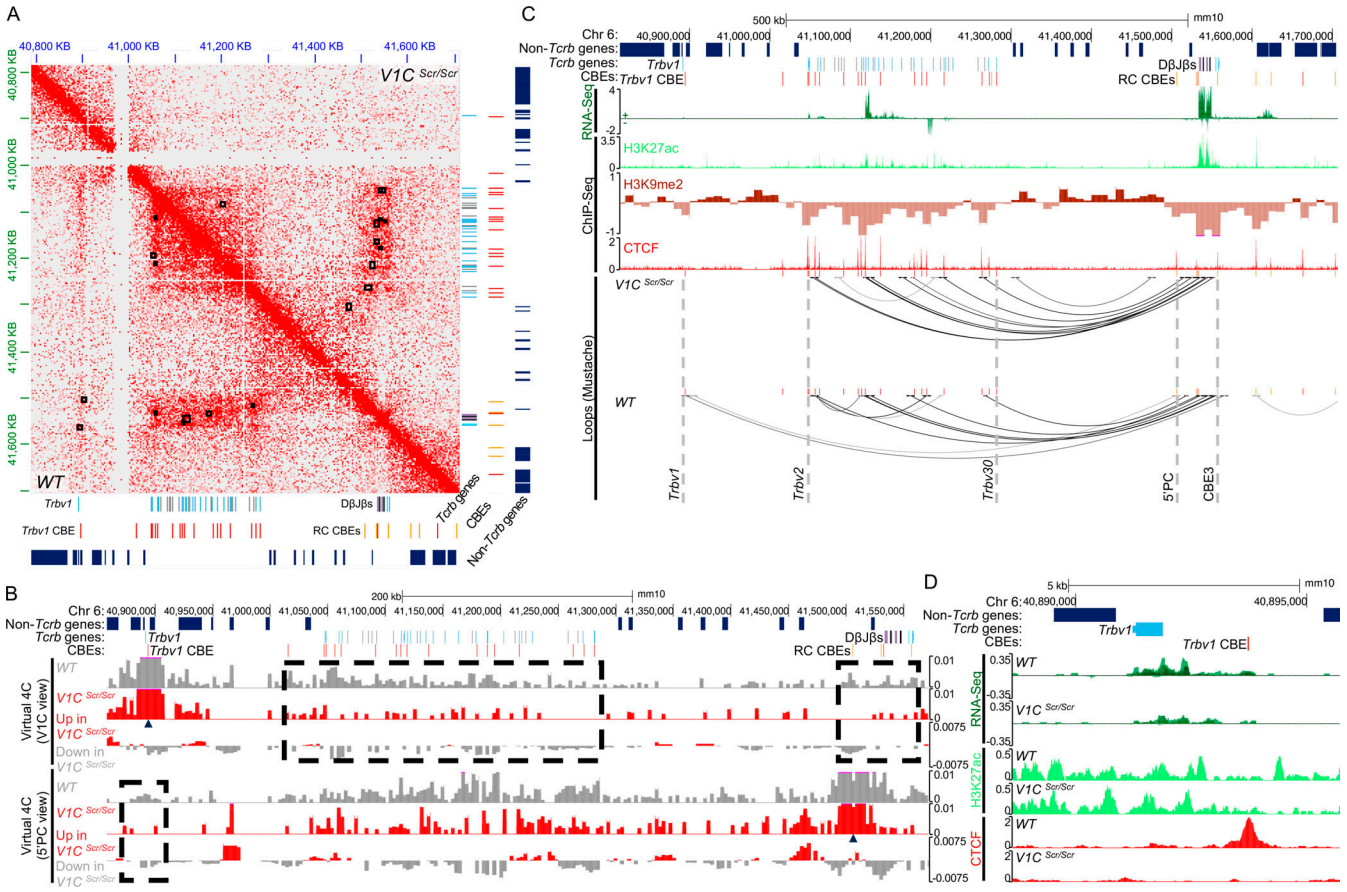

Figure 3. **The *Trbv1* CBE stimulates recombination by anchoring and terminating loop extrusion. (A)** HiC heat maps of *Tcrb* loci in thymocytes from $V1C^{Scr/Scr}Rag1^{-/-}$ ($V1C^{Scr/Scr}$) or $Rag1^{-/-}$ (*WT*) mice. Data are combined from two independent experiments, each performed on cells pooled from at least five $V1C^{Scr/Scr}$ or *WT* mice of either sex and presented at 3 kb resolution. Each panel indicates loops (black squares) identified by MUSTACHE performed at 3, 5, or 10 kb resolution. **(B)** Virtual 4C tracks of the *Trbv1* CBE or 5′PC viewpoint from $V1C^{Scr/Scr}$ or *WT* thymocytes generated from HiC data of panel A. Black arrowheads below indicate the 4C viewpoint. The bottom track for each viewpoint shows $V1C^{Scr/Scr}$ data subtracted by *WT* data so that signals above the axis (red) or below the axis (gray) indicate contacts that are greater in $V1C^{Scr/Scr}$ or *WT* cells, respectively. Differentially interacting regions are boxed. **(C)** Genome browser views depicting two replicates each of RNA-Seq (sense and antisense transcripts) or a representative of two replicates of ChIP-Seq for H3K27ac, H3K9me2, or CTCF of *Tcrb* loci from $V1C^{Scr/Scr}$ thymocytes, or MUSTACHE loops on $V1C^{Scr/Scr}$ (top) or *WT* (bottom) thymocytes shown in panel A. RNA-Seq and ChIP-Seq data are shown as reads per million, except for H3K9me2, which is shown as the $\log_2$ ratio of bound H3K9me2 over input control (enriched for = brown above axis; depletion of = light brown below axis). **(D)** Genome browser views depicting representative RNA-Seq (sense and antisense transcripts) or ChIP-Seq for H3K27ac or CTCF spanning the *Trbv1* region in *WT* or $V1C^{Scr/Scr}$ thymocytes. RNA-Seq and ChIP-Seq data are shown as reads per million.

extrusion anchored at RCs to progress linearly to *Trbv1*. Indeed, loop extrusion anchored at the *Trbv1* CBE would reel the RC region toward Vβ RSSs rather than move Vβ RSSs past the unoccupied active site of RAG-bound RCs—the foundation of RAG scanning (Fig. 6). Thus, *Trbv1*-anchored loop extrusion, as well as homotypic interactions, are expected to position *Trbv1* and RC RSSs close enough to facilitate diffusion-based synapsis, which is orientation independent.

HiC heatmaps from RAG-deficient lymphocytes provide information regarding topological regulation of AgR loci and potential mechanisms for synapsis of RSSs across enormous genomic distances. However, the only current means of determining whether diffusion-based synapsis can mediate a V-to-(D)J recombination event at *Trbv1* is to invert the genomic orientation of its RSS (Dai et al., 2021; Hill et al., 2020; Zhao et al., 2016). Any inversional rearrangements between the reoriented RSS and its normal partner(s) must occur by diffusion-based synapsis, not by active RAG scanning. To determine whether *Tcrb* can employ diffusion-based synapsis for *Trbv1* recombination, we first replaced its RSS with a more efficient version (3′Dβ1 RSS) in either the normal (Wu et al., 2022) or inverted orientation (the $V1^{R}$ or $V1^{Ri}$ allele, respectively; Fig. 5 A). As sequences flanking an RSS influence recombination (Boubnov et al., 1995; Gerstein and Lieber, 1993; Hesse et al., 1989; Nadel et al., 1998; Yu and Lieber, 1999), we inserted the last 10 nucleotides of *Trbv1* coding sequence fused to the inverted 3′Dβ1 RSS (Fig. 5 A). As expected, the $V1^{R/R}$ allele rearranged efficiently to produce TRBV1^{+} thymocytes, whereas $V1^{Ri/Ri}$ mice lack TRBV1^{+} αβ T cells because any inversional rearrangement would fail to create a functional *Tcrb* gene (Fig. 5, B and C). To quantify inversional *Trbv1* rearrangements in the engineered mice, we used Taqman quantitative PCR (qPCR) on DNA isolated from DN3 thymocytes. No inversional rearrangements were found in $V1^{R/R}$ thymocytes because the RSS orientation only permits

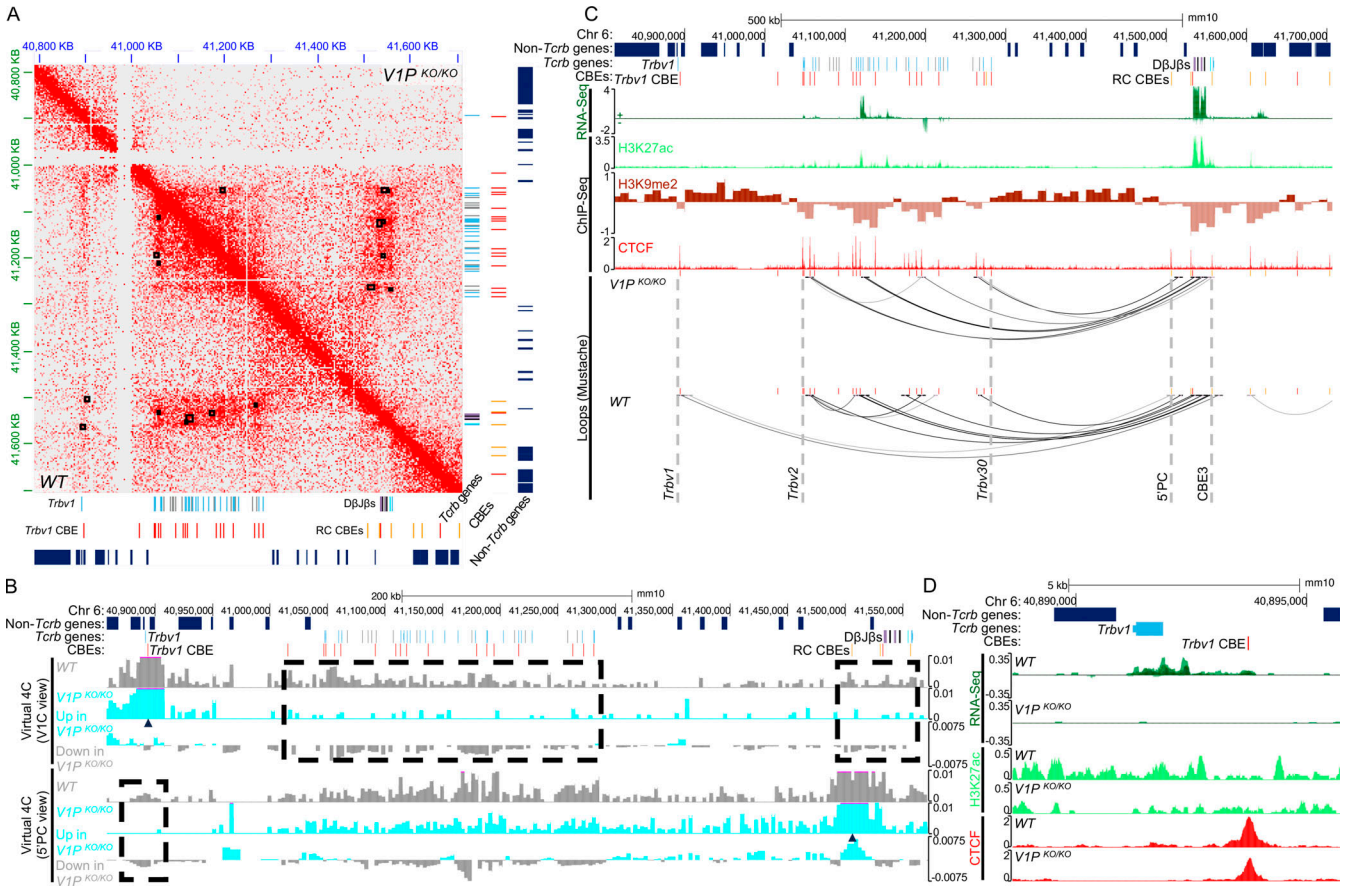

Figure 4. **Promoter-mediated homotypic chromatin interactions drive *Trbv1* rearrangement. (A)** HiC heat maps of *Tcrb* loci in thymocytes from *V1P*$^{KO/KO}$*Rag1*$^{-/-}$ (*V1P*$^{KO/KO}$) or *Rag1*$^{-/-}$ (*WT*) mice. Data are combined from two independent experiments, each performed on cells pooled from at least five *V1P*$^{KO/KO}$ or *WT* mice of either sex and presented at 3 kb resolution. Each panel indicates loops (black squares) identified by MUSTACHE performed at 3, 5, or 10 kb resolution. **(B)** Virtual 4C tracks of the *Trbv1* CBE or 5′PC viewpoint from *V1P*$^{KO/KO}$ or *WT* thymocytes generated from HiC data of panel A. The black arrowheads below indicate the 4C viewpoint. The bottom track for each viewpoint shows *V1P*$^{KO/KO}$ data subtracted by *WT* data so that signals above the axis (cyan) or below the axis (gray) indicate contacts that are greater in *V1P*$^{KO/KO}$ or *WT* cells, respectively. Differentially interacting regions are boxed. **(C)** Genome browser views depicting two replicates each of RNA-Seq (sense and antisense transcripts) or a representative of two replicates of ChIP-Seq for H3K27ac, H3K9me2, or CTCF of *Tcrb* loci from *V1P*$^{KO/KO}$ thymocytes, or MUSTACHE loops on *V1P*$^{KO/KO}$ (top) or *WT* (bottom) thymocytes shown in panel A. RNA-Seq and ChIP-Seq data are shown as reads per million, except for H3K9me2, which is shown as the $\log_2$ ratio of bound H3K9me2 over input control (enriched for = brown above axis; depletion of = light brown below axis). **(D)** Genome browser views depicting representative RNA-Seq (sense and antisense transcripts) or ChIP-Seq for H3K27ac or CTCF spanning the *Trbv1* region in *WT* or *V1P*$^{KO/KO}$ thymocytes. RNA-Seq and ChIP-Seq data are shown as reads per million.

deletional recombination (Fig. 5 D). In contrast, signal joins and coding joins created by inversions were detected in *V1*$^{Ri/Ri}$ thymocytes (Fig. 5 D). Notably, these inversions occurred with Dβ1Jβ1 segments (Fig. 5 D), indicating that *Tcrb* can support long-range primary Vβ rearrangement through diffusion-based synapsis.

To determine the relative levels of inversional versus deletional *Trbv1* rearrangements on *V1*^{Ri} alleles and *V1*^{R} alleles, respectively, we developed a Taqman assay to quantify RAG cleavage at each RSS. Using primers that anneal to sequences surrounding each *Trbv1* RSS, we can detect RAG cleavage by loss of the amplification signal (Fig. 5 E). Applying this assay to sorted DN3 thymocytes, we detected cleavage at 16.6% of *V1*^{Ri} alleles, compared with 31.7% cleavage at *V1*^{R} alleles (Fig. 5 F). These data demonstrate that inversional events on *V1*^{Ri} alleles proceed at a frequency comparable to deletional events on *V1*^{R} alleles. Accordingly, *Tcrb* can employ diffusion-based synapsis to mediate long-range V-to-(D)J recombination, in addition to potential unidirectional RAG scanning from the RC as at *Igh* loci (Ba et al., 2020; Dai et al., 2021; Hill et al., 2020; Jain et al., 2018; Zhang et al., 2019). Thus, we conclude that the pathways involved in folding a given AgR locus determine the range of mechanisms deployed for long-range RSS synapsis and, likely, contribute to V gene segment usage in primary Ig and TCR repertoires.

Discussion

The folding of chromosomes is a dynamic process that creates topological domains to control numerous biological processes by promoting or inhibiting functional interactions between distal DNA elements. We examined how these dynamic mechanisms impact long-range contacts within *Tcrb* loci, a critical aspect of their assembly into functional AgR genes during T cell

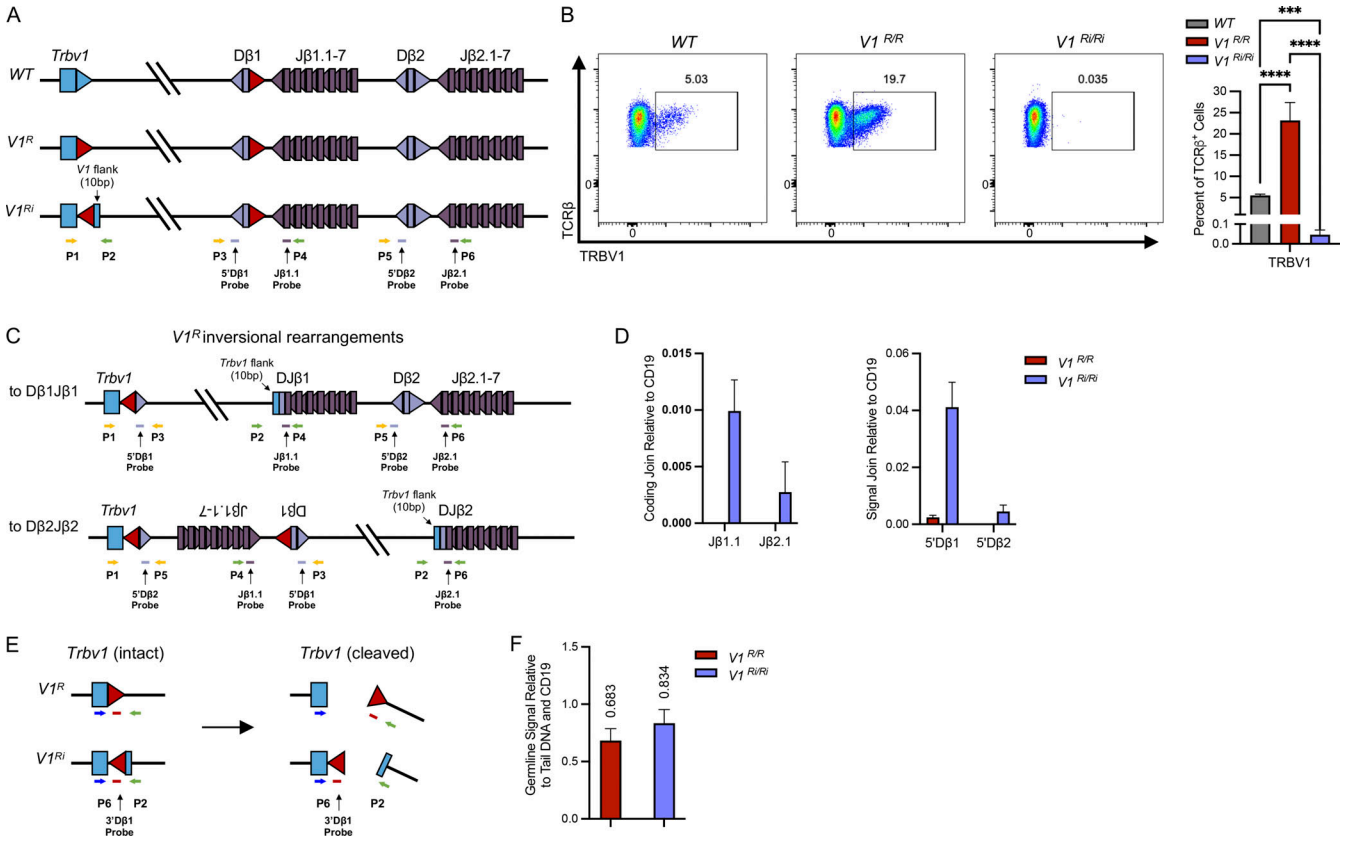

Figure 5. ***Tcrb* employs diffusion-based synapsis as an underlying mechanism of V(D)J recombination. (A)** Schematic representation of the *Trbv1* and DβJβ genomic regions of the *Tcrb* allele of mice with the *Trbv1* RSS in native configuration (*WT*) or replacement of the *Trbv1* RSS with the 3′Dβ1 RSS in the same ($V1^{R}$) or inverted ($V1^{Ri}$) genomic orientation. The locations of PCR primers used to analyze *Tcrb* rearrangement coding joins (green arrows) or signal joins (orange arrows) with relevant probes (purple lines) in each genotype are depicted below the $V1^{Ri}$ allele. **(B)** Representative flow cytometry plots (left) and quantification (right) of thymic αβ T cells expressing TRBV1⁺ TCRβ proteins on their surface in *WT*, $V1^{R/R}$, and $V1^{Ri/Ri}$ mice. *n* = 6; one-way ANOVA followed by Tukey's post-tests for multiple comparisons. ***P < 0.001 and ****P < 0.0001. **(C)** Schematic representation of $V1^{Ri}$ alleles with rearrangement between the inverted 3′Dβ1 RSS at *Trbv1* and the 5′Dβ1 RSS (top) or 5′Dβ2 RSS (bottom). The locations of PCR primers used to analyze *Tcrb* rearrangement coding joins (green arrows) or signal joins (orange arrows) with relevant probes (purple lines) are indicated. **(D)** Taqman PCR quantification of indicated coding joins (left) or signal joins (right) generated by inversional rearrangements between the inverted 3′Dβ1 RSS at *Trbv1* and the 5′ Dβ1 RSS or 5′Dβ2 RSS. *n* = 5. **(E)** Schematic representation of primer and probe placement for cleavage assay. **(F)** Taqman PCR quantification of cleavage assay where the plotted frequency represents intact alleles normalized to uncut alleles (tail DNA) and CD19. *n* = 4, 6.

development. We found that homotypic chromatin interactions and bidirectional chromosome loop extrusion both contribute to long-range contacts in *Tcrb* loci, enabling efficient recombination between distal Vβ and DβJβ gene segments. Integrated analysis of our new -omics data supported an important role for homotypic chromatin interactions in establishing contact domains, with robust interactions between transcriptionally active chromatin at the *Trbv1* segment, the main Vβ cluster, and the RC region, and segregation of these domains from intervening stretches of silent chromatin. Our work also supported roles for bidirectional loop extrusion initiating from the RC or upstream Vβ segments in distinct cells for folding *Tcrb*, with resulting chromosome loops placing these Vβ segments near the RC region.

The independent contributions of chromosome loops and homotypic chromatin interactions in forming *Tcrb* structures and driving its recombination were tested by directed mutations of the most distal Vβ gene segment, *Trbv1*. Deletion of the *Trbv1*-proximal CBE revealed that it serves a dual role at *Tcrb*—acting as a primary anchor for loop extrusion originating at or near this distal gene segment and as a terminal anchor for extrusion emanating from the RC. Accordingly, loss of this single CBE severely diminished locus-wide *Trbv1* contacts and its recombination, despite retaining substantial levels of transcription and active chromatin. In this regard, inactivation of the *Trbv1* promoter confirmed that a transcriptionally active chromatin environment was critical for its long-range contacts with the main Vβ cluster and with the RC. Indeed, these contacts were retained at a residual level in the CBE but not in the promoter mutant, suggesting that homotypic interactions of active *Trbv1* chromatin can drive some long-range contacts independent of loop anchoring, the *Trbv1* promoter can act as an alternative anchor for cohesin-mediated loop extrusion, or both. HiC heatmaps from the promoter mutant are consistent with a multifaceted role for this cis element, serving as an anchor for *Trbv1*→RC loop extrusion, driving *Trbv1* compartmentalization to favor its stable interaction with other CBEs, and enabling the nearby CBE to be a terminal anchor for RC→*Trbv1* loop extrusion. Finally, we

directly tested how these architectural mechanisms determine the range of substrates that can be utilized by RAG complexes to generate AgR genes. Inversion of the *Trbv1*-RSS continued to support its long-range recombination with DβJβ clusters at an appreciable level, precluding RAG scanning from the RC as the sole mechanism for *Tcrb* rearrangement. Indeed, these findings further substantiate the involvement of bidirectional loop extrusion, in combination with homotypic chromatin interactions, as vehicles for promoting diffusion-based contacts between distal elements.

Our study also highlights the range of mechanisms employed by developing lymphocytes to ensure efficient assembly of Ig and TCR genes, while also normalizing usage of V segments that are spread over large chromosomal distances from the RC. Prior studies have elegantly shown that *Igh* is folded in pro-B cells predominantly by unidirectional, cohesin-driven loop extrusion emanating from the D_H-J_H-C_H end of the locus, progressing upstream into the large span of V_H chromatin (Ba et al., 2020; Bhat et al., 2023; Dai et al., 2021; Hill et al., 2020, 2023; Jain et al., 2018; Zhang et al., 2019). This means of locus folding promotes RAG scanning of V_H segments, as the latter spool past the open active site of RC-bound RAG complexes, restricting recombination to only convergently oriented RSSs (Dai et al., 2021; Hill et al., 2020). In this mechanism, V_H CBEs act as a pause for loop extrusion rather than anchors that generate loops to enhance the frequency of diffusion-based synapsis (Dai et al., 2021; Hill et al., 2020). Similarly, our contact maps indicate that one facet of *Tcrb* folding is a cohesin-driven loop extrusion originating from the RC and progressing through *Trbv1*, which is consistent with its use of RAG scanning for long-range rearrangements. However, unlike *Igh*, loop extrusion also originates at high frequencies in the V chromatin regions of *Tcrb*, progressing in the opposite direction, toward the RC. Together with homotypic chromatin interactions, this bidirectional loop extrusion should allow for diffusion-based synapsis in an RSS orientation-independent manner. Indeed, in marked contrast to *Igh*, flipping the linear genomic orientation of the RSS attached to *Trbv1* enables recombination through inversion, which is not possible by RAG scanning (Dai et al., 2021; Hill et al., 2020). Recent studies have shown that folding of *Igk* in pre-B cells is accomplished by loop extrusion from RC-proximal CBEs proceeding up through the large Vκ cluster, as well as loop extrusion that is confined within the Vκ cluster (Hill et al., 2023). This contrasts with *Tcrb* where frequent loop extrusion originating in the Vβ regions proceeds down through the RC. The dual origins of loop extrusion in *Igk* form multiple adjacent Vκ loops and a single Jκ-Cκ loop that positions Vκ segments near the RC. Creation of this architecture likely is important to facilitate diffusion-based synapsis at *Igk* since its assembly can occur by either inversional or deletional Vκ-to-Jκ recombination, depending on RSS orientations (Hill et al., 2023).

It remains an open question as to why *Tcrb* employs mechanisms that promote diffusion-based synapsis given that all upstream Vβ gene segments have RSSs oriented convergently with their partner RSSs in the RC, rearranging by deletion. Perhaps diffusion augments the frequency of long-range contacts that would arise during RAG scanning to enhance overall recombination efficiencies. Alternatively, a chromosome loop existing before RAG binding establishes an RC might increase the efficiency of RAG scanning by providing a structure that facilitates loop extrusion by cohesin anchored at RAG or other features of RC chromatin. Another intriguing possibility may derive from the unique structure of *Tcrb*, which has two Dβ-Jβ-Cβ clusters and a solitary Vβ gene segment, *Trbv31*, which lies downstream of the RC and rearranges by inversion. In DN thymocytes that harbor a non-functional Vβ31-Dβ1Jβ1 coding join, secondary recombination is permitted between upstream Vβs and the Dβ2Jβ cluster (Lee and Bassing, 2020). However, in this configuration, all remaining Vβ RSSs and their Dβ2 RSS target are in an identical linear orientation, and any secondary rearrangements must occur by inversion, necessitating diffusion-mediated synapsis.

Our data, coupled with previous observations, support a layered model for the folding of *Tcrb* into structures that favor long-range Vβ contacts and recombination in DN thymocytes. First, the Eβ super-enhancer engages germline Dβ promoters to generate transcriptionally activated chromatin over DβJβ clusters, enabling RAG binding, RC formation, and DβJβ recombination. Concurrently, promoter-dependent transcription of each Vβ gene segment generates active chromatin locally and renders each downstream RSS accessible to RAG. Simultaneous activation of Vβ and DβJβ chromatin drives homotypic chromatin interactions to stabilize spatial proximity when these regions encounter one another during loop extrusion. In that regard, Eβ, Dβ, and some Vβ promoters likely serve as loading sites for cohesin, which migrates randomly back and forth until it is impeded by CTCF at RC or Vβ CBEs, or by RAG at a DβJβ complex, which then prompts cohesin-driven extrusion in either direction. Regardless of direction, extrusion anchored at an RC or Vβ CBE can terminate at the opposite element, generating a loop that juxtaposes DβJβ complexes and Vβ segments to facilitate their recombination by diffusion-based synapsis (Fig. 6). It is also likely that collision of converging extrusion events forms side-by-side loops that similarly promote long-range Vβ-to-DβJβ recombination. These structure-forming mechanisms likely occur on top of RAG scanning, as loop extrusion anchored at the RC and progressing into Vβ chromatin allows RAG to unidirectionally scan for an accessible Vβ RSS (Fig. 6).

Our discovery, linking distinct mechanisms of folding with recombination at *Tcrb*, has important implications for other biological processes. As one example, current evidence suggests that during the cellular response to a DNA double-strand break (DSB), cohesin is anchored at each DNA end. Cohesin docking activates unidirectional loop extrusion that allows histone H2Ax phosphorylation (forming γ-H2Ax) by the ATM kinase as chromatin is reeled past kinases at the damage site (Arnould et al., 2021). This process creates γ-H2Ax domains around DSBs that promote end-joining by holding together DNA ends (Yin et al., 2009). The apparent importance of homotypic chromatin interactions in forming *Tcrb* structures could explain why DSBs within the locus produce γ-H2Ax patterns that reproduce intralocus contacts, presumably by interacting with DSB-proximal ATM, rather than simply spreading out linearly from the break. Specifically, γ-H2Ax accumulates at much

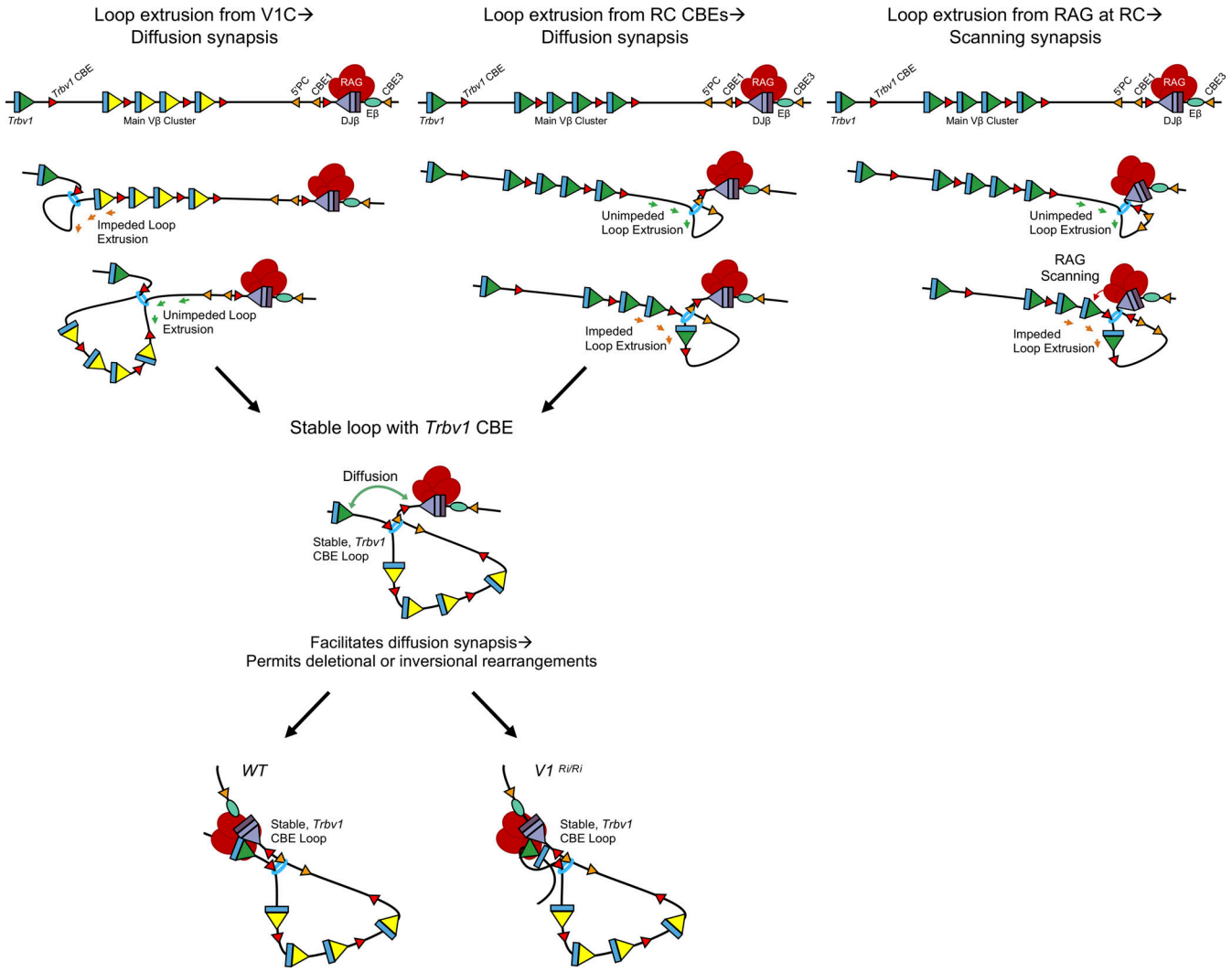

Figure 6. **The mechanisms of *Tcrb* folding determine modes of long-range Vβ recombination.** Left: Loop extrusion emanating from the *Trbv1* CBE promotes rearrangement of only *Trbv1* by generating chromosome loops with RC CBEs, positioning *Trbv1* in spatial proximity with the RC to facilitate diffusion-based synapsis. Homotypic chromatin interactions between active *Trbv1* and RC chromatin stabilize these loops to increase the chance for synapsis. Center: Loop extrusion emanating from an RC CBE promotes rearrangement of upstream Vβ segments by forming chromosome loops with any convergent Vβ CBE, juxtaposing adjacent Vβ segments and the RC to facilitate diffusion-based synapsis. Homotypic chromatin interactions between active RC and Vβ chromatin stabilize these loops to increase the chance for synapsis. Right: Loop extrusion anchored by an RC promotes rearrangement of upstream Vβ segments by enabling the open active site of RAG bound at a DβJβ complex RSS to scan Vβ chromatin for synapsis with a Vβ RSS. Impediments to cohesin activity in Vβ chromatin, including homotypic interactions with RC chromatin, enhance the ability of RAG scanning to capture a Vβ RSS. Depicted in all panels are *Tcrb* gene segments as rectangles (Vβ, blue; Dβ, lavender; Jβ,purple) and RSSs as triangles (Dβ and Jβ RSSs match their gene segment color; Vβ RSSs are colored according to their availability [green] or unavailability [yellow] for synapsis and rearrangement), CBEs as triangles (red = sense strand; orange = antisense strand), cohesin as a ring (cyan), Eβ as an oval (teal), and RAG (dark red).

higher levels across the interacting active chromatin regions than intervening silent heterochromatin regions (Collins et al., 2020). Thus, either DSBs induced within *Tcrb* do not activate loop extrusion emanating from each DNA end or homotypic chromatin interactions stabilize contacts during this process to locally increase γ-H2Ax. Beyond orchestrating DNA recombination and repair, regulation of anchoring sites and directions of loop extrusion contributes to proper expression of complex genetic loci at specific developmental stages, including those encoding globin, homeobox, protocadherin, and olfactory receptor genes. Approaches like those employed here can be used to study the contributions of directional loop extrusion and homotypic chromatin interactions toward contacts between the requisite cis-acting elements in health and disease.

Materials and methods

Mice

Mice used for all experiments were 4–6 wk old, of mixed sex, and housed under specific pathogen–free conditions at the Children's Hospital of Philadelphia (CHOP) or the Ohio State University (OSU) College of Medicine. All animal husbandry, breeding, and experiments were performed in accordance with national guidelines and regulations and approved by the CHOP

Institutional Animal Care and Use Committee and the OSU Institutional Animal Care and Use Committee. Wild-type (C57BL/6J) and *Rag1*$^{-/-}$(B6.129S7-*Rag1*^{tm1Mom}/J) mice were obtained from Jackson Laboratories. The *V1*$^{R/R}$ mice were previously described (Wu et al., 2022). We used the Easi-CRISPR method (Quadros et al., 2017) of CRISPR/Cas9-mediated genomic editing in C57BL/6 zygotes to create mice with a scrambled *Trbv1* CBE (*V1C*^{Scr} allele), a deletion of the *Trbv1* promoter (*V1P*^{KO} allele), or an inverted 3′Dβ1RSS replacement of the *Trbv1* RSS (*V1*^{Ri} allele).

For the *V1C*$^{Scr/Scr}$ mice, we used CRISPOR to identify a suitable guide sequence on the antisense strand to position the cut site centrally within the *Trbv1* CBE. The crispr RNA (crRNA) was purchased from Integrated DNA Technologies (IDT) with the identified guide sequence (see Table S3 for a complete list of oligos). The Easi-CRISPR method uses single stranded DNA as donors (ssODN) for homology-directed repair, which carried a previously published scrambled CBE sequence that was confirmed not to bind CTCF (Jain et al., 2018). The CHOP Transgenic Core electroporated zygotes with a mixture of ctRNA (8 µM; crRNA + trans-activating crispr RNA [tracrRNA]), Cas9 protein (3.2 µM), ssODN (20 µM) in Duplex Buffer diluted 1:1 with Opti-MEM buffer. A similar approach was used to generate the *V1P*$^{KO/KO}$ mice, with the exception that two different guide RNAs were used to generate a deletion between the two cut sites, with no homology-directed repair. The mixture used to electroporate zygotes contained two different ctRNAs (4 µM each; two different crRNAs independently annealed to tracrRNA) and no ssODN. For the *V1*$^{Ri/Ri}$ mice, we utilized the same crRNA as in a previous study to replace the *Trbv1* RSS with the 3′Dβ1 RSS in its normal orientation (*V1*^{R}; Wu et al., 2022). This crRNA targets the sense strand within the spacer of the *Trbv1* RSS. The ssODN harbors the 3′Dβ1 RSS in the inverted orientation plus 10 bases of *Trbv1* flanking sequence. *V1C*$^{Scr/Scr}$ founders were screened by PCR of tail DNA with the V1Cdelta5′ and CBEScrRev or CBEScrFwd and V1Cdelta3′ primers to test for the presence of the scrambled sequence and to check for appropriate insertion of the 5′ and 3′ homology arms, respectively. *V1P*$^{KO/KO}$ founders were screened with the V1PKO5′ and V1PKO3′ primers, which span the region we targeted for deletion. Finally, *V1*$^{Ri/Ri}$ founders were screened with the V1RSSComFwd and 3′Dβ1Fwd or 3′Dβ1Rev and V1RSSComRev primers. For each mutant, two founder lines were selected and backcrossed to *WT* mice for two generations to ensure the propagation of a single validated mutant allele and limit potential off-target CRISPR effects. We crossed heterozygous F2 mice to generate homozygous mice, and genotypes were verified by PCR with the flanking primers, followed by Sanger Sequencing from either end of the PCR product. The sequence-validated founder lines were analyzed by flow cytometry using *WT* littermate controls to confirm the same phenotype between founder lines. One line was selected for Adaptive Immunosequencing analysis and to backcross onto the RAG-deficient background.

HiC

Four replicates of conventional HiC were performed on *Rag1*$^{-/-}$ mouse thymocytes as previously described (Collins et al., 2020; Rao et al., 2014). Briefly, 5 × 10^6 formaldehyde-crosslinked DN cells were lysed with 250 µl of ice-cold HiC lysis buffer (10 mM Tris-HCl, pH 8.0, 10 mM NaCl, 0.2% IGEPAL CA630) containing protease inhibitors (Roche) for 15 min on ice. Chromatin was digested at 37°C for 6 h with DpnII (100 U); ends were filled and marked with biotin using Klenow and ligated together with T4 DNA ligase. Following the reversal of crosslinking, DNA was fragmented on a Covaris E220 Evolution Sonicator and size-selected for 300–500 bp with AMPure XP Beads (Beckman Coulter). DNA ends were repaired with the NEBNext Ultra II DNA Library Prep Kit according to the manufacturer's instructions using 1 µg of the HiC DNA. The adapter-ligated DNA was size-selected for 300–400 bp with AMPure XP beads and biotinylated DNA fragments were pulled down using MyOne Streptavidin T1 beads (Life Technologies). The final HiC library was generated with 5 PCR cycles using the NEBNext Ultra II DNA Library Prep Kit and NEBNext Dual Index primers (NEB) for Illumina sequencing. For comparison of our mutants, we performed two replicates each with RAG-deficient thymocytes of the *WT*, *V1C*$^{Scr/Scr}$, or *V1P*$^{KO/KO}$ background using the Arima-HiC Kit (A510008) according to the manufacture's protocol with the KAPA Hyper Prep Kit. We performed these HiC on cells pooled from at least five mice for each genotype. Paired-end sequencing for both HiC methods was performed on an Illumina NovaSeq 6000 (300 cycles) and specific read depths were provided (Table S1).

RNA-Seq

RNA-Seq was performed on sorted (B220$^-$, CD19$^-$, CD11b$^-$, CD11c$^-$, NK1.1$^-$, TER119$^-$, TCRβ$^-$, and TCRγ/δ$^-$) DN thymocytes from two *Rag1*$^{-/-}$ mice per experiment (see Table S4 for the list of antibodies). RNA extraction, library preparations, sequencing reactions, and bioinformatics analysis were conducted at GENEWIZ, LLC. Total RNA was extracted from frozen cell pellet samples using Qiagen Rneasy Plus Universal mini kit following the manufacturer's instructions (Qiagen). RNA samples were quantified using Qubit 2.0 Fluorometer (Life Technologies) and RNA integrity was checked with 4200 TapeStation (Agilent Technologies). RNA-Seq library preparation was prepared using Rib0-Zero rRNA Removal Kit and TruSeq Stranded Total RNA library Prep kit following the manufacturer's protocol (RS-122-2101; Illumina). Briefly, rRNA was depleted with Ribp-Zero rRNA Removal Kit. rRNA-depleted RNAs were fragmented for 8 min at 94°C. First-strand and second-strand cDNA were subsequently synthesized. The second strand of cDNA was marked by incorporating dUTP during the synthesis. cDNA fragments were adenylated at 3′ends and the indexed adapter was ligated to cDNA fragments. Limited cycle PCR was used for library enrichment. The incorporated dUTP in second-strand cDNA quenched the amplification of the second strand, which helped to preserve the strand specificity. Sequencing libraries were validated using DNA Analysis Screen Tape on the Agilent 2200 TapeStation (Agilent Technologies) and quantified by using Qubit 2.0 Fluorometer (Invitrogen) as well as by qPCR (Applied Biosystems). The sequencing libraries were multiplexed and clustered on three lanes of a flowcell. After clustering, the flowcell was loaded on the Illumina HiSeq instrument according to the manufacturer's instructions. The samples were sequenced using a 2 × 150 Pair-End High Output configuration. Image analysis and base calling were conducted by the HiSeq Control Software on the

HiSeq instrument. Raw sequence data (.bcl files) generated from Illumina HiSeq were converted into fastq files and demultiplexed using Illumina bcl2fastq program version 2.17. One mismatch was allowed for index sequence identification.

ChIP-Seq

ChIP-Seq was performed on DN thymocytes pooled from five to seven mice of mixed sex of the RAG-deficient background. 10 million cells were fixed with 2% formaldehyde in complete RPMI media (10% FBS, 1% Pen/Strep) for 5 min (CTCF) or 1% formaldehyde for 10 min (histone marks) at room temperature on an orbital shaker. The crosslinking reaction was quenched with glycine at a final concentration of 120 mM for 5 min on ice and then washed once with PBS. Fixed cells were then resuspended in nuclei isolation buffer (10 mM Tris-HCl, pH 7.5, 10 mM NaCl, 1% IGEPAL) with protease inhibitors (5871S; Cell Signaling Technology) and incubated with rotation at 4°C for 10 min. Next, nuclei were lysed with SDS lysis buffer (1% SDS; 10 mMM EDTA; 50 mM Tris-HCl, pH 8) with protease inhibitor for 20 min on ice and then sonicated with a Diagenode Bioruptor for 20 cycles (1 cycle = 30 s on, 30 s off). Sonicated lysate was spun down to remove cellular debris. At this stage, portions were set aside for input control and confirmation of successful sonication. The rest was diluted with ChIP dilution buffer (0.01% SDS; 1.1% Triton X-100; 1.2 mM EDTA; 16.7 mM Tris-HCl, pH 8; and 167 mM NaCl) plus protease inhibitors and then split between four preprepared antibody–protein A bead conjugates (including an IgG control). Protein A beads (ab214286; Abcam) were washed three times with PBS/T (PBS with 0.02% Tween) and then incubated with rotation for at least 4 h at 4°C with antibody in PBS/T (see Table S4 for a list of antibodies). Following incubation, bead–antibody conjugate was washed three times with PBS/T, added to diluted, sonicated chromatin, and incubated with rotation overnight at 4°C. Next day, the supernatant was aspirated off and the beads were washed with rotation at 4°C for three min each with low salt wash (0.1% SDS; 1% Triton X-100; 2 mM EDTA; 20 mM Tris-HCl, pH 8; 150 mM NaCl), high salt wash (0.1% SDS; 1% Triton X-100; 2 mM EDTA; 20 mM Tris-HCl, pH 8; 500 mM NaCl), LiCl wash (0.25 M LiCl; 1% IGEPAL; 1% sodium deoxycholate; 1 mM EDTA; 10 mM Tris-HCl, pH 8), and then twice with Tris EDTA buffer. Chromatin was then eluted from the beads in two rounds with 50 µl of freshly prepared elution buffer (1% SDS 0.1 M $NaHCO_3$) at 56°C with rotation. Elute was treated with RNAseA (R1253; Thermo Fisher Scientific) for 4 h and then proteinase K (BP1700100; Thermo Fisher Scientific) overnight at 56°C. Decrosslinked DNA was purified using AMPure XP beads and libraries were generated with the NEBNext Ultra II DNA Library Prep Kit for Illumina (E7645). Libraries were pooled for a target of 20 million (CTCF) or 40 million (histone marks) paired-end reads per sample and sequenced on an Illumina NovaSeq 6000 (200 or 300 cycles). For Rad21 ChIP, we used publicly available data (GSM2973690; Loguercio et al., 2018) and ran it through our computational analysis pipeline.

Computational analyses

For HiC, paired-end raw reads were mapped with bwa version (Li and Durbin, 2009), treating forward and reverse reads separately, as described and implemented with the HiCExplorer command tool version 3.6 (Ramírez et al., 2018). For Fig. 1, we combined experimental data from conventional and Arima HiC because they had sufficient pairwise Spearman correlations. For Figs. 3 and 4, we downsampled data from the genotype with the most reads to be equivalent to the number of reads from the genotype with the least reads. Visualization was done via the UCSC genome browser (Kent et al., 2002), using the interact format and juicebox (Robinson et al., 2019). MUSTACHE version 1.2.0 (Roayaei Ardakany et al., 2020) was used to identify significant looping at resolutions 10, 5, and 3 K. Raw RNA-Seq reads were trimmed using bbduk as part of bbmap (version 38.92; https://sourceforge.net/projects/bbmap/). Reads were then aligned to mm10 using STAR (version 2.7.9a; Dobin et al., 2013). bamCoverage from the deeptools package (version 3.5.1; Ramírez et al., 2016) yielded the bigwig coverage files and was run using flags to separate the coverage tracks by strandedness and to normalize to counts per million. Normalized bigwig coverage files were uploaded to the UCSC genome browser (Keng et al., 2002).

For ChiP-Seq, paired-end reads were aligned to the mm10 genome using bowtie2 (version 2.4.5; Langmead and Salzberg, 2012). Peak calling was done using the macs2 algorithm (version 2.2.7.1; Zhang et al., 2008), with an exception for the H3K9me2 mark where the edd (version 1.1.9) software (Lund et al., 2014) was used to identify enriched domains. Bigwig files for the visualization in the UCSC genome browser were yielded by the bamCoverage tool inside the deeptools package (version 3.5.1; Ramírez et al., 2016) applying the reads per genomic content normalization. Finally, the bioconductor package chipqc (version 1.30.0; Carroll et al., 2014) that helped determine our samples had a Reads in Peaks score of at least 4.

Flow cytometry

Flow cytometry was performed on thymocytes from individual mice. Single-cell suspensions were prepared and treated with red blood cell lysis buffer (140 mM NH_4Cl; 17 mM Tris, pH 7.4). Fc receptors were blocked with anti-CD16/CD32 and antibodies were stained in PBS with 2% FBS and 2 mM EDTA. To determine any effect on gross αβ T cell development and expression of TCRβ chains utilizing the *Trbv1* gene segment, we stained with the following panel: CD4, CD8, TCRβ, Vβ2 (TRBV1), and live/dead aqua (L34957; Life Technologies). Data were collected on an LSR Fortessa and analyzed with FlowJo software. Single cells were gated based on forward and side scatter. For statistical analyses, we performed one-way ANOVA followed by Tukey's post-tests for multiple comparisons.

Adaptive Immunosequencing

Adaptive Immunosequencing was performed on sorted DN3 thymocytes ($CD4^-$, $CD8^-$, $B220^-$, $CD19^-$, $CD11b^-$, $CD11c^-$, $NK1.1^-$, $TER119^-$, $TCR\beta^-$, $TCR\gamma/\delta^-$, $CD44^-$, and $CD25^+$) pooled from two mice per experiment. Genomic DNA was isolated using the DNeasy Blood and Tissue Kit (69506; Qiagen) and submitted to Adaptive Biotechnologies for their Mouse TCRβ assay at the survey resolution. Read depths for each sample are listed (Table S2). For statistical analyses, we performed multiple unpaired t-tests.

Real-time qPCR

TaqMan qPCR was performed with PrimeTime Gene Expression Master Mix (1055772; IDT) on sorted DN3 thymocytes (CD4⁻, CD8⁻, B220⁻, CD19⁻, CD11b⁻, CD11c⁻, NK1.1⁻, TER119⁻, TCRβ⁻, TCRγ/δ⁻, CD44⁻, and CD25⁺) from two RAG-sufficient mice per experiment. Primer/probe placement to assay for rearrangements (Fig. 5 A) was designed to amplify both coding joins and signal joins resulting from inversional rearrangement to either DJβ1.1 or DJβ2.1 (Fig. 5 C). This PCR strategy will also amplify any inversional rearrangements directly to Jβ1.1 or Jβ2.1. Primer/probe placement to assay for cleavage at *Trbv1* (Fig. 5 E) was designed to span the RSS in both $Vl^{R/R}$ and $Vl^{Ri/Ri}$ alleles such that a loss in amplification signal corresponds with RAG cleavage.

Online supplemental material

Table S1 lists sequencing details for all HiC samples, showing numbers of sequenced reads, numbers, and percentages of paired mappable reads, and numbers and percentages of HiC contact reads. Table S2 lists sequencing details for all Adaptive Immunosequencing samples, showing numbers of total unique complete *Tcrb* rearrangements, numbers of unique *Trbv1* rearrangements, and percentages of *Tcrb* rearrangements involving *Trbv1*. Table S3 lists all oligo sequences for generation of genotyping of mouse lines, as well as qPCR. Table S4 lists all antibodies used for the indicated experiment.

Data availability

The data in Figs. 1, 3, and 4 are openly available in NCBI's Gene Expression Omnibus and are accessible through GEO Series accession number GSE249649.

Acknowledgments

We thank Adele Harman of the CHOP Transgenic Core for establishing all of the novel genetically modified mouse strains in this study.

Support provided by National Institutes of Health grants R01 AI130231 (E.M. Oltz and C.H. Bassing), R37 AI118852 (E.M. Oltz), and R21 AI174545 (C.H. Bassing).

Author contributions: E.M. Oltz and C.H. Bassing designed and supervised the study. K. Lee and B.M. Allyn created and analyzed the $Vl^{KO/KO}$ and $Vlc^{Scr/Scr}$ mice by flow cytometry and Adaptive Immunosequencing. B.M. Allyn bred $Vl^{KO/KO}$ and $Vlc^{Scr/Scr}$ mice onto the RAG-deficient background and conducted Arima HiC, RNA-Seq, or ChIP-Seq on thymocytes. C. Oyeniran and V. Nganga performed conventional HiC experiments and library preparation for Arima HiC and ChIP-Seq. K.E. Hayer conducted all computational analyses and helped B.M. Allyn prepare figures. A. Sacan mentored K.E. Hayer on computational data. B.M. Allyn wrote the manuscript and prepared figures under the guidance of E.M. Oltz and C.H. Bassing, who worked together to edit the assembled manuscript.

Disclosures: The authors declare no competing interests exist.

Submitted: 7 June 2023
Revised: 12 October 2023
Accepted: 15 December 2023

References

Allyn, B.M., K.D. Lee, and C.H. Bassing. 2020. Genome topology control of antigen receptor gene assembly. *J. Immunol.* 204:2617–2626. https://doi.org/10.4049/jimmunol.1901356

Arnould, C., V. Rocher, A.L. Finoux, T. Clouaire, K. Li, F. Zhou, P. Caron, P.E. Mangeot, E.P. Ricci, R. Mourad, et al. 2021. Loop extrusion as a mechanism for formation of DNA damage repair foci. *Nature*. 590:660–665. https://doi.org/10.1038/s41586-021-03193-z

Ba, Z., J. Lou, A.Y. Ye, H.Q. Dai, E.W. Dring, S.G. Lin, S. Jain, N. Kyritsis, K.R. Kieffer-Kwon, R. Casellas, and F.W. Alt. 2020. CTCF orchestrates long-range cohesin-driven V(D)J recombinational scanning. *Nature*. 586:305–310. https://doi.org/10.1038/s41586-020-2578-0

Barajas-Mora, E.M., L. Lee, H. Lu, J.A. Valderrama, E. Bjanes, V. Nizet, A.J. Feeney, M. Hu, and C. Murre. 2023. Enhancer-instructed epigenetic landscape and chromatin compartmentalization dictate a primary antibody repertoire protective against specific bacterial pathogens. *Nat. Immunol.* 24:320–336. https://doi.org/10.1038/s41590-022-01402-z

Barrington, C., D. Georgopoulou, D. Pezic, W. Varsally, J. Herrero, and S. Hadjur. 2019. Enhancer accessibility and CTCF occupancy underlie asymmetric TAD architecture and cell type specific genome topology. *Nat. Commun.* 10:2908. https://doi.org/10.1038/s41467-019-10725-9

Bassing, C.H., W. Swat, and F.W. Alt. 2002. The mechanism and regulation of chromosomal V(D)J recombination. *Cell*. 109 Suppl:S45–S55. https://doi.org/10.1016/s0092-8674(02)00675-x

Bassing, C.H., S. Whitlow, R. Mostoslavsky, K. Yang-Iott, S. Ranganath, and F.W. Alt. 2008. Vbeta cluster sequences reduce the frequency of primary Vbeta2 and Vbeta14 rearrangements. *Eur. J. Immunol.* 38:2564–2572. https://doi.org/10.1002/eji.200838347

Bhat, K.H., S. Priyadarshi, S. Naiyer, X. Qu, H. Farooq, E. Kleiman, J. Xu, X. Lei, J.F. Cantillo, R. Wuerffel, et al. 2023. An Igh distal enhancer modulates antigen receptor diversity by determining locus conformation. *Nat. Commun.* 14:1225. https://doi.org/10.1038/s41467-023-36414-2

Boija, A., I.A. Klein, B.R. Sabari, A. Dall'Agnese, E.L. Coffey, A.V. Zamudio, C.H. Li, K. Shrinivas, J.C. Manteiga, N.M. Hannett, et al. 2018. Transcription factors activate genes through the phase-separation capacity of their activation domains. *Cell*. 175:1842–1855.e16. https://doi.org/10.1016/j.cell.2018.10.042

Boubnov, N.V., Z.P. Wills, and D.T. Weaver. 1995. Coding sequence composition flanking either signal element alters V(D)J recombination efficiency. *Nucleic Acids Res.* 23:1060–1067. https://doi.org/10.1093/nar/23.6.1060

Busslinger, G.A., R.R. Stocsits, P. van der Lelij, E. Axelsson, A. Tedeschi, N. Galjart, and J.M. Peters. 2017. Cohesin is positioned in mammalian genomes by transcription, CTCF and Wapl. *Nature*. 544:503–507. https://doi.org/10.1038/nature22063

Carroll, T.S., Z. Liang, R. Salama, R. Stark, and I. de Santiago. 2014. Impact of artifact removal on ChIP quality metrics in ChIP-seq and ChIP-exo data. *Front Genet.* 5:75. https://doi.org/10.3389/fgene.2014.00075

Carico, Z., and M.S. Krangel. 2015. Chromatin dynamics and the development of the TCRα and TCRδ repertoires. *Adv. Immunol.* 128:307–361. https://doi.org/10.1016/bs.ai.2015.07.005

Chong, S., C. Dugast-Darzacq, Z. Liu, P. Dong, G.M. Dailey, C. Cattoglio, A. Heckert, S. Banala, L. Lavis, X. Darzacq, and R. Tjian. 2018. Imaging dynamic and selective low-complexity domain interactions that control gene transcription. *Science*. 361:eaar2555. https://doi.org/10.1126/science.aar2555

Collins, P.L., C. Purman, S.I. Porter, V. Nganga, A. Saini, K.E. Hayer, G.L. Gurewitz, B.P. Sleckman, J.J. Bednarski, C.H. Bassing, and E.M. Oltz. 2020. DNA double-strand breaks induce H2Ax phosphorylation domains in a contact-dependent manner. *Nat. Commun.* 11:3158. https://doi.org/10.1038/s41467-020-16926-x

Csink, A.K., and S. Henikoff. 1996. Genetic modification of heterochromatic association and nuclear organization in Drosophila. *Nature*. 381:529–531. https://doi.org/10.1038/381529a0

Dai, H.Q., H. Hu, J. Lou, A.Y. Ye, Z. Ba, X. Zhang, Y. Zhang, L. Zhao, H.S. Yoon, A.M. Chapdelaine-Williams, et al. 2021. Loop extrusion mediates physiological Igh locus contraction for RAG scanning. *Nature*. 590:338–343. https://doi.org/10.1038/s41586-020-03121-7

Davidson, I.F., B. Bauer, D. Goetz, W. Tang, G. Wutz, and J.M. Peters. 2019. DNA loop extrusion by human cohesin. *Science*. 366:1338–1345. https://doi.org/10.1126/science.aaz3418

de Wit, E., E.S.M. Vos, S.J.B. Holwerda, C. Valdes-Quezada, M.J.A.M. Verstegen, H. Teunissen, E. Splinter, P.J. Wijchers, P.H. Krijger, and W. de Laat. 2015. CTCF binding polarity determines chromatin looping. *Mol. Cell*. 60:676–684. https://doi.org/10.1016/j.molcel.2015.09.023

Delmonte, O.M., C. Schuetz, and L.D. Notarangelo. 2018. RAG deficiency: Two genes, many diseases. *J. Clin. Immunol.* 38:646–655. https://doi.org/10.1007/s10875-018-0537-4

Dixon, J.R., S. Selvaraj, F. Yue, A. Kim, Y. Li, Y. Shen, M. Hu, J.S. Liu, and B. Ren. 2012. Topological domains in mammalian genomes identified by analysis of chromatin interactions. *Nature*. 485:376–380. https://doi.org/10.1038/nature11082

Dobin, A., C.A. Davis, F. Schlesinger, J. Drenkow, C. Zaleski, S. Jha, P. Batut, M. Chaisson, T.R. Gingeras. 2013. STAR: ultrafast universal RNA-seq aligner. *Bioinformatics*. 29:15–21. https://doi.org/10.1093/bioinformatics/bts635

Dowen, J.M., Z.P. Fan, D. Hnisz, G. Ren, B.J. Abraham, L.N. Zhang, A.S. Weintraub, J. Schujiers, T.I. Lee, K. Zhao, and R.A. Young. 2014. Control of cell identity genes occurs in insulated neighborhoods in mammalian chromosomes. *Cell*. 159:374–387. https://doi.org/10.1016/j.cell.2014.09.030

Eagen, K.P. 2018. Principles of chromosome architecture revealed by hi-C. *Trends Biochem. Sci.* 43:469–478. https://doi.org/10.1016/j.tibs.2018.03.006

Ebert, A., L. Hill, and M. Busslinger. 2015. Spatial regulation of V-(D)J recombination at antigen receptor loci. *Adv. Immunol.* 128:93–121. https://doi.org/10.1016/bs.ai.2015.07.006

Falk, M., Y. Feodorova, N. Naumova, M. Imakaev, B.R. Lajoie, H. Leonhardt, B. Joffe, J. Dekker, G. Fudenberg, I. Solovei, and L.A. Mirny. 2019. Heterochromatin drives compartmentalization of inverted and conventional nuclei. *Nature*. 570:395–399. https://doi.org/10.1038/s41586-019-1275-3

Flavahan, W.A., Y. Drier, B.B. Liau, S.M. Gillespie, A.S. Venteicher, A.O. Stemmer-Rachamimov, M.L. Suvà, and B.E. Bernstein. 2016. Insulator dysfunction and oncogene activation in IDH mutant gliomas. *Nature*. 529:110–114. https://doi.org/10.1038/nature16490

Fudenberg, G., M. Imakaev, C. Lu, A. Goloborodko, N. Abdennur, and L.A. Mirny. 2016. Formation of chromosomal domains by loop extrusion. *Cell Rep.* 15:2038–2049. https://doi.org/10.1016/j.celrep.2016.04.085

Fuxa, M., J. Skok, A. Souabni, G. Salvagiotto, E. Roldan, and M. Busslinger. 2004. Pax5 induces V-to-DJ rearrangements and locus contraction of the immunoglobulin heavy-chain gene. *Genes Dev.* 18:411–422. https://doi.org/10.1101/gad.291504

Ganai, N., S. Sengupta, and G.I. Menon. 2014. Chromosome positioning from activity-based segregation. *Nucleic Acids Res.* 42:4145–4159. https://doi.org/10.1093/nar/gkt1417

Gerstein, R.M., and M.R. Lieber. 1993. Coding end sequence can markedly affect the initiation of V(D)J recombination. *Genes Dev.* 7:1459–1469. https://doi.org/10.1101/gad.7.7b.1459

Gopalakrishnan, S., K. Majumder, A. Predeus, Y. Huang, O.I. Koues, J. Verma-Gaur, S. Loguercio, A.I. Su, A.J. Feeney, M.N. Artyomov, and E.M. Oltz. 2013. Unifying model for molecular determinants of the preselection Vβ repertoire. *Proc. Natl. Acad. Sci. USA*. 110:E3206–E3215. https://doi.org/10.1073/pnas.1304048110

Gotzmann, J., and R. Foisner. 1999. Lamins and lamin-binding proteins in functional chromatin organization. *Crit. Rev. Eukaryot. Gene Expr.* 9:257–265. https://doi.org/10.1615/CritRevEukarGeneExpr.v9.i3-4.100

Harrison, R.E.S., K. Weng, Y. Wang, and Q. Peng. 2021. Phase separation and histone epigenetics in genome regulation. *Curr. Opin. Solid State Mater. Sci.* 25:100892. https://doi.org/10.1016/j.cossms.2020.100892

Hesse, J.E., M.R. Lieber, K. Mizuuchi, and M. Gellert. 1989. V(D)J recombination: A functional definition of the joining signals. *Genes Dev.* 3:1053–1061. https://doi.org/10.1101/gad.3.7.1053

Hilbert, L., Y. Sato, K. Kuznetsova, T. Bianucci, H. Kimura, F. Jülicher, A. Honigmann, V. Zaburdaev, and N.L. Vastenhouw. 2021. Transcription organizes euchromatin via microphase separation. *Nat. Commun.* 12:1360. https://doi.org/10.1038/s41467-021-21589-3

Hildebrand, E.M., and J. Dekker. 2020. Mechanisms and functions of chromosome compartmentalization. *Trends Biochem. Sci.* 45:385–396. https://doi.org/10.1016/j.tibs.2020.01.002

Hill, L., A. Ebert, M. Jaritz, G. Wutz, K. Nagasaka, H. Tagoh, D. Kostanova-Poliakova, K. Schindler, Q. Sun, P. Bönelt, et al. 2020. Wapl repression by Pax5 promotes V gene recombination by Igh loop extrusion. *Nature*. 584:142–147. https://doi.org/10.1038/s41586-020-2454-y

Hill, L., G. Wutz, M. Jaritz, H. Tagoh, L. Calderón, J.M. Peters, A. Goloborodko, and M. Busslinger. 2023. Igh and Igk loci use different folding principles for V gene recombination due to distinct chromosomal architectures of pro-B and pre-B cells. *Nat. Commun.* 14:2316. https://doi.org/10.1038/s41467-023-37994-9

Hnisz, D., A.S. Weintraub, D.S. Day, A.L. Valton, R.O. Bak, C.H. Li, J. Goldmann, B.R. Lajoie, Z.P. Fan, A.A. Sigova, et al. 2016. Activation of proto-oncogenes by disruption of chromosome neighborhoods. *Science*. 351:1454–1458. https://doi.org/10.1126/science.aad9024

Jain, S., Z. Ba, Y. Zhang, H.Q. Dai, and F.W. Alt. 2018. CTCF-binding elements mediate accessibility of RAG substrates during chromatin scanning. *Cell*. 174:102–116.e14. https://doi.org/10.1016/j.cell.2018.04.035

Jeppsson, K., T. Sakata, R. Nakato, S. Milanova, K. Shirahige, and C. Björkegren. 2022. Cohesin-dependent chromosome loop extrusion is limited by transcription and stalled replication forks. *Sci. Adv.* 8:eabn7063. https://doi.org/10.1126/sciadv.abn7063

Jhunjhunwala, S., M.C. van Zelm, M.M. Peak, S. Cutchin, R. Riblet, J.J.M. van Dongen, F.G. Grosveld, T.A. Knoch, and C. Murre. 2008. The 3D structure of the immunoglobulin heavy-chain locus: Implications for long-range genomic interactions. *Cell*. 133:265–279. https://doi.org/10.1016/j.cell.2008.03.024

Ji, X., D.B. Dadon, B.E. Powell, Z.P. Fan, D. Borges-Rivera, S. Shachar, A.S. Weintraub, D. Hnisz, G. Pegoraro, T.I. Lee, et al. 2016. 3D chromosome regulatory landscape of human pluripotent cells. *Cell Stem Cell*. 18:262–275. https://doi.org/10.1016/j.stem.2015.11.007

Ji, Y., A.J. Little, J.K. Banerjee, B. Hao, E.M. Oltz, M.S. Krangel, and D.G. Schatz. 2010a. Promoters, enhancers, and transcription target RAG1 binding during V(D)J recombination. *J. Exp. Med.* 207:2809–2816. https://doi.org/10.1084/jem.20101136

Ji, Y., W. Resch, E. Corbett, A. Yamane, R. Casellas, and D.G. Schatz. 2010b. The in vivo pattern of binding of RAG1 and RAG2 to antigen receptor loci. *Cell*. 141:419–431. https://doi.org/10.1016/j.cell.2010.03.010

Kagey, M.H., J.J. Newman, S. Bilodeau, Y. Zhan, D.A. Orlando, N.L. Van Berkum, C.C. Ebmeier, J. Goossens, P.B. Rahl, S.S. Levine. 2010. Mediator and cohesin connect gene expression and chromatin architecture. *Nature*. 467:430–435. https://doi.org/10.1038/nature09380

Kent, W.J., C.W. Sugnet, T.S. Furey, K.M. Roskin, T.H. Pringle, A.M. Zahler, and D. Haussler. 2002. The human genome browser at UCSC. *Genome Res.* 12:996–1006. https://doi.org/10.1101/gr.229102

Kenter, A.L., and A.J. Feeney. 2019. New insights emerge as antibody repertoire diversification meets chromosome conformation. *F1000Res.* 8:F1000 Faculty Rev-347. https://doi.org/10.12688/f1000research.17358.1

Kim, Y., Z. Shi, H. Zhang, I.J. Finkelstein, and H. Yu. 2019. Human cohesin compacts DNA by loop extrusion. *Science*. 366:1345–1349. https://doi.org/10.1126/science.aaz4475

Kosak, S.T., J.A. Skok, K.L. Medina, R. Riblet, M.M. Le Beau, A.G. Fisher, and H. Singh. 2002. Subnuclear compartmentalization of immunoglobulin loci during lymphocyte development. *Science*. 296:158–162. https://doi.org/10.1126/science.1068768

Krangel, M.S. 2003. Gene segment selection in V(D)J recombination: accessibility and beyond. *Nat. Immunol.* 4:624–630. https://doi.org/10.1038/ni0703-624

Langmead, B., and S.L. Salzberg. 2012. Fast gapped-read alignment with Bowtie 2. *Nat Methods*. 9:357–359. https://doi.org/10.1038/nmeth.1923

Lee, K.D., and C.H. Bassing. 2020. Two successive inversional Vβ rearrangements on a single Tcrb allele can contribute to the TCRβ repertoire. *J. Immunol.* 204:78–86. https://doi.org/10.4049/jimmunol.1901105

Li, H.,and R. Durbin. 2009. Fast and accurate short read alignment with Burrows-Wheeler transform. *Bioinformatics*. 25:1754–1760. https://doi.org/10.1093/bioinformatics/btp324

Li, G., X. Ruan, R.K. Auerbach, K.S. Sandhu, M. Zheng, P. Wang, H.M. Poh, Y. Goh, J. Lim, J. Zhang, et al. 2012. Extensive promoter-centered chromatin interactions provide a topological basis for transcription regulation. *Cell*. 148:84–98. https://doi.org/10.1016/j.cell.2011.12.014

Li, Y., J.H.I. Haarhuis, Á. Sedeño Cacciatore, R. Oldenkamp, M.S. van Ruiten, L. Willems, H. Teunissen, K.W. Muir, E. de Wit, B.D. Rowland, and D. Panne. 2020. The structural basis for cohesin-CTCF-anchored loops. *Nature*. 578:472–476. https://doi.org/10.1038/s41586-019-1910-z

Loguercio, S., E.M. Barajas-Mora, H.Y. Shih, M.S. Krangel, and A.J. Feeney. 2018. Variable extent of lineage-specificity and developmental stage-specificity of cohesin and CCCTC-binding factor binding within the immunoglobulin and cell receptor loci. *Front. Immunol.* 9:425. https://doi.org/10.3389/fimmu.2018.00425

Lund, E., R. Oldenburg, and P. Collas. 2014. Enriched domain detector: a program for detection of wide genomic enrichment domains robust against local variations. *Nucleic Acids Res.* 42:e92. https://doi.org/10.1093/nar/gku324

Lupiáñez, D.G., K. Kraft, V. Heinrich, P. Krawitz, F. Brancati, E. Klopocki, D. Horn, H. Kayserili, J.M. Opitz, R. Laxova, et al. 2015. Disruptions of topological chromatin domains cause pathogenic rewiring of gene-enhancer interactions. *Cell*. 161:1012–1025. https://doi.org/10.1016/j.cell.2015.04.004

Luppino, J.M., and E.F. Joyce. 2020. Single cell analysis pushes the boundaries of TAD formation and function. *Curr. Opin. Genet. Dev.* 61:25–31. https://doi.org/10.1016/j.gde.2020.03.005

Majumder, K., C.H. Bassing, and E.M. Oltz. 2015a. Regulation of Tcrb gene assembly by genetic, epigenetic, and topological mechanisms. *Adv. Immunol.* 128:273–306. https://doi.org/10.1016/bs.ai.2015.07.001

Majumder, K., O.I. Koues, E.A.W. Chan, K.E. Kyle, J.E. Horowitz, K. Yang-Iott, C.H. Bassing, I. Taniuchi, M.S. Krangel, and E.M. Oltz. 2015b. Lineage-specific compaction of Tcrb requires a chromatin barrier to protect the function of a long-range tethering element. *J. Exp. Med.* 212:107–120. https://doi.org/10.1084/jem.20141479

Mathieu, N., W.M. Hempel, S. Spicuglia, C. Verthuy, and P. Ferrier. 2000. Chromatin remodeling by the T cell receptor (TCR)-β gene enhancer during early T cell development: Implications for the control of TCR-β locus recombination. *J. Exp. Med.* 192:625–636. https://doi.org/10.1084/jem.192.5.625

McMillan, R.E., and M.L. Sikes. 2008. Differential activation of dual promoters alters Dbeta2 germline transcription during thymocyte development. *J. Immunol.* 180:3218–3228. https://doi.org/10.4049/jimmunol.180.5.3218

Mirny, L.A., M. Imakaev, and N. Abdennur. 2019. Two major mechanisms of chromosome organization. *Curr. Opin. Cell Biol.* 58:142–152. https://doi.org/10.1016/j.ceb.2019.05.001

Nadel, B., A. Tang, G. Escuro, G. Lugo, and A.J. Feeney. 1998. Sequence of the spacer in the recombination signal sequence affects V(D)J rearrangement frequency and correlates with nonrandom Vkappa usage in vivo. *J. Exp. Med.* 187:1495–1503. https://doi.org/10.1084/jem.187.9.1495

Narendra, V., P.P. Rocha, D. An, R. Raviram, J.A. Skok, E.O. Mazzoni, and D. Reinberg. 2015. CTCF establishes discrete functional chromatin domains at the Hox clusters during differentiation. *Science*. 347:1017–1021. https://doi.org/10.1126/science.1262088

Penagos-Puig, A., and M. Furlan-Magaril. 2020. Heterochromatin as an important driver of genome organization. *Front. Cell Dev. Biol.* 8:579137. https://doi.org/10.3389/fcell.2020.579137

Proudhon, C., B. Hao, R. Raviram, J. Chaumeil, and J.A. Skok. 2015. Long-range regulation of V(D)J recombination. *Adv Immunol.* 128:123–182. https://doi.org/10.1016/bs.ai.2015.07.003

Quadros, R.M., H. Miura, D.W. Harms, H. Akatsuka, T. Sato, T. Aida, R. Redder, G.P. Richardson, Y. Inagaki, D. Sakai, et al. 2017. Easi-CRISPR: A robust method for one-step generation of mice carrying conditional and insertion alleles using long ssDNA donors and CRISPR ribonucleoproteins. *Genome Biol.* 18:92. https://doi.org/10.1186/s13059-017-1220-4

Ramírez, F., D.P. Ryan, B. Grüning, V. Bhardwaj, F. Kilpert, A.S. Richter, S. Heyne, F. Dündar, and T. Manke. 2016. deepTools2: A next generation web server for deep-sequencing data analysis. *Nucleic Acids Res.* 44: W160–W165. https://doi.org/10.1093/nar/gkw257

Ramírez, F., V. Bhardwaj, L. Arrigoni, K.C. Lam, B.A. Grüning, J. Villaveces, B. Habermann, A. Akhtar, and T. Manke. 2018. High-resolution TADs reveal DNA sequences underlying genome organization in flies. *Nat. Commun.* 9:189. https://doi.org/10.1038/s41467-017-02525-w

Ranganath, S., A.C. Carpenter, M. Gleason, A.C. Shaw, C.H. Bassing, and F.W. Alt. 2008. Productive coupling of accessible Vbeta14 segments and DJbeta complexes determines the frequency of Vbeta14 rearrangement. *J. Immunol.* 180:2339–2346. https://doi.org/10.4049/jimmunol.180.4.2339

Rao, S.S.P., M.H. Huntley, N.C. Durand, E.K. Stamenova, I.D. Bochkov, J.T. Robinson, A.L. Sanborn, I. Machol, A.D. Omer, E.S. Lander, and E.L. Aiden. 2014. A 3D map of the human genome at kilobase resolution reveals principles of chromatin looping. *Cell*. 159:1665–1680. https://doi.org/10.1016/j.cell.2014.11.021

Ribeiro de Almeida, C., R.W. Hendriks, and R. Stadhouders. 2015. Dynamic control of long-range genomic interactions at the immunoglobulin κ light-chain locus. *Adv. Immunol.* 128:183–271. https://doi.org/10.1016/bs.ai.2015.07.004

Roayaei Ardakany, A., H.T. Gezer, S. Lonardi, and F. Ay. 2020. Mustache: multi-scale detection of chromatin loops from Hi-C and Micro-C maps using scale-space representation. *Genome Biol.* 21:256. https://doi.org/10.1186/s13059-020-02167-0

Robinson, J.T., D. Turner, N.C. Durand, H. Thorvaldsdóttir, J.P. Mesirov, and E.L. Aiden. 2019. Juicebox.js provides a cloud-based visualization system for Hi-C data. *Cell Syst.* 6:256–258.e1. https://doi.org/10.1016/j.cels.2018.01.001

Roldán, E., M. Fuxa, W. Chong, D. Martinez, M. Novatchkova, M. Busslinger, and J.A. Skok. 2005. Locus "decontraction" and centromeric recruitment contribute to allelic exclusion of the immunoglobulin heavy-chain gene. *Nat. Immunol.* 6:31–41. https://doi.org/10.1038/ni1150

Rowley, M.J., and V.G. Corces. 2018. Organizational principles of 3D genome architecture. *Nat. Rev. Genet.* 19:789–800. https://doi.org/10.1038/s41576-018-0060-8

Rowley, M.J., M.H. Nichols, X. Lyu, M. Ando-Kuri, I.S.M. Rivera, K. Hermetz, P. Wang, Y. Ruan, and V.G. Corces. 2017. Evolutionarily conserved principles predict 3D chromatin organization. *Mol. Cell*. 67:837–852.e7. https://doi.org/10.1016/j.molcel.2017.07.022

Sakamoto, S., K. Wakae, Y. Anzai, K. Murai, N. Tamaki, M. Miyazaki, K. Miyazaki, W.J. Romanow, T. Ikawa, D. Kitamura, et al. 2012. E2A and CBP/p300 act in synergy to promote chromatin accessibility of the immunoglobulin κ locus. *J. Immunol.* 188:5547–5560. https://doi.org/10.4049/jimmunol.1002346

Sanborn, A.L., S.S.P. Rao, S.C. Huang, N.C. Durand, M.H. Huntley, A.I. Jewett, I.D. Bochkov, D. Chinnappan, A. Cutkosky, J. Li, et al. 2015. Chromatin extrusion explains key features of loop and domain formation in wild-type and engineered genomes. *Proc. Natl. Acad. Sci. USA*. 112: E6456–E6465. https://doi.org/10.1073/pnas.1518552112

Schatz, D.G., and P.C. Swanson. 2011. V(D)J recombination: Mechanisms of initiation. *Annu. Rev. Genet.* 45:167–202. https://doi.org/10.1146/annurev-genet-110410-132552

Schlissel, M.S. 2004. Regulation of activation and recombination of the murine Igkappa locus. *Immunol. Rev.* 200:215–223. https://doi.org/10.1111/j.0105-2896.2004.00157.x

Seitan, V.C., B. Hao, K. Tachibana-Konwalski, T. Lavagnolli, H. Mira-Bontenbal, K.E. Brown, G. Teng, T. Carroll, A. Terry, K. Horan, et al. 2011. A role for cohesin in T-cell-receptor rearrangement and thymocyte differentiation. *Nature*. 476:467–471. https://doi.org/10.1038/nature10312

Shih, H.Y., and M.S. Krangel. 2010. Distinct contracted conformations of the Tcra/Tcrd locus during Tcra and Tcrd recombination. *J. Exp. Med.* 207: 1835–1841. https://doi.org/10.1084/jem.20100772

Shih, H.Y., J. Verma-Gaur, A. Torkamani, A.J. Feeney, N. Galjart, and M.S. Krangel. 2012. Tcra gene recombination is supported by a Tcra enhancer- and CTCF-dependent chromatin hub. *Proc. Natl. Acad. Sci. USA*. 109:E3493–E3502. https://doi.org/10.1073/pnas.1214131109

Sikes, M.L., A. Meade, R. Tripathi, M.S. Krangel, and E.M. Oltz. 2002. Regulation of V(D)J recombination: A dominant role for promoter positioning in gene segment accessibility. *Proc. Natl. Acad. Sci. USA*. 99: 12309–12314. https://doi.org/10.1073/pnas.182166699

Skok, J.A., R. Gisler, M. Novatchkova, D. Farmer, W. de Laat, and M. Busslinger. 2007. Reversible contraction by looping of the Tcra and Tcrb loci in rearranging thymocytes. *Nat. Immunol.* 8:378–387. https://doi.org/10.1038/ni1448

Sleckman, B.P., J.R. Gorman, and F.W. Alt. 1996. Accessibility control of antigen-receptor variable-region gene assembly: Role of cis-acting elements. *Annu. Rev. Immunol.* 14:459–481. https://doi.org/10.1146/annurev.immunol.14.1.459

Verma-Gaur, J., A. Torkamani, L. Schaffer, S.R. Head, N.J. Schork, and A.J. Feeney. 2012. Noncoding transcription within the Igh distal V(H) region at PAIR elements affects the 3D structure of the Igh locus in pro-B cells. *Proc. Natl. Acad. Sci. USA*. 109:17004–17009. https://doi.org/10.1073/pnas.1208398109

Vian, L., A. Pękowska, S.S.P. Rao, K.R. Kieffer-Kwon, S. Jung, L. Baranello, S.C. Huang, L. El Khattabi, M. Dose, N. Pruett, et al. 2018. The energetics and physiological impact of cohesin extrusion. *Cell*. 173:1165–1178.e20. https://doi.org/10.1016/j.cell.2018.03.072

Wang, L., Y. Gao, X. Zheng, C. Liu, S. Dong, R. Li, G. Zhang, Y. Wei, H. Qu, Y. Li, et al. 2019. Histone modifications regulate chromatin compartmentalization by contributing to a phase separation mechanism. *Mol. Cell*. 76:646–659.e6. https://doi.org/10.1016/j.molcel.2019.08.019

Whitehurst, C.E., S. Chattopadhyay, and J. Chen. 1999. Control of V(D)J recombinational accessibility of the D β 1 gene segment at the TCR β locus by a germline promoter. *Immunity*. 10:313–322. https://doi.org/10.1016/S1074-7613(00)80031-X

Wu, C., C.H. Bassing, D. Jung, B.B. Woodman, D. Foy, and F.W. Alt. 2003. Dramatically increased rearrangement and peripheral representation of Vbeta14 driven by the 3'Dbeta1 recombination signal sequence. *Immunity*. 18:75–85. https://doi.org/10.1016/S1074-7613(02)00515-0

Wu, C., S. Ranganath, M. Gleason, B.B. Woodman, T.M. Borjeson, F.W. Alt, and C.H. Bassing. 2007. Restriction of endogenous T cell antigen receptor beta rearrangements to Vbeta14 through selective recombination signal sequence modifications. *Proc. Natl. Acad. Sci. USA*. 104: 4002–4007. https://doi.org/10.1073/pnas.0700081104

Wu, G.S., E.J. Culberson, B.M. Allyn, and C.H. Bassing. 2022. Poor-Quality Vβ recombination signal sequences and the DNA damage response ATM kinase collaborate to establish TCRβ gene repertoire and allelic exclusion. *J. Immunol.* 208:2583–2592. https://doi.org/10.4049/jimmunol.2100489

Wu, G.S., K.S. Yang-Iott, M.A. Klink, K.E. Hayer, K.D. Lee, and C.H. Bassing. 2020. Poor quality Vβ recombination signal sequences stochastically

enforce TCRβ allelic exclusion. *J. Exp. Med.* 217:e20200412. https://doi.org/10.1084/jem.20200412

Wutz, G., C. Várnai, K. Nagasaka, D.A. Cisneros, R.R. Stocsits, W. Tang, S. Schoenfelder, G. Jessberger, M. Muhar, M.J. Hossain, et al. 2017. Topologically associating domains and chromatin loops depend on cohesin and are regulated by CTCF, WAPL, and PDS5 proteins. *EMBO J.* 36: 3573–3599. https://doi.org/10.15252/embj.201798004

Yin, B., V. Savic, M.M. Juntilla, A.L. Bredemeyer, K.S. Yang-Iott, B.A. Helmink, G.A. Koretzky, B.P. Sleckman, and C.H. Bassing. 2009. Histone H2AX stabilizes broken DNA strands to suppress chromosome breaks and translocations during V(D)J recombination. *J. Exp. Med.* 206: 2625–2639. https://doi.org/10.1084/jem.20091320

Yu, K., and M.R. Lieber. 1999. Mechanistic basis for coding end sequence effects in the initiation of V(D)J recombination. *Mol. Cell Biol.* 19: 8094–8102. https://doi.org/10.1128/MCB.19.12.8094

Zhang, Y., T. Liu, C.A. Meyer, J. Eeckhoute, D.S. Johnson, B.E. Bernstein, C. Nusbaum, R.M. Myers, M. Brown, W. Li, and X.S. Liu. 2008. Model-based analysis of ChIP-Seq (MACS). *Genome Biol.* 9:R137. https://doi.org/10.1186/gb-2008-9-9-r137

Zhang, Y., X. Zhang, Z. Ba, Z. Liang, E.W. Dring, H. Hu, J. Lou, N. Kyritsis, J. Zurita, M.S. Shamim, et al. 2019. The fundamental role of chromatin loop extrusion in physiological V(D)J recombination. *Nature.* 573: 600–604. https://doi.org/10.1038/s41586-019-1547-y

Zhang, Y., X. Zhang, H.Q. Dai, H. Hu, and F.W. Alt. 2022. The role of chromatin loop extrusion in antibody diversification. *Nat. Rev. Immunol.* 22: 550–566. https://doi.org/10.1038/s41577-022-00679-3

Zhao, L., R.L. Frock, Z. Du, J. Hu, L. Chen, M.S. Krangel, and F.W. Alt. 2016. Orientation-specific RAG activity in chromosomal loop domains contributes to Tcrd V(D)J recombination during T cell development. *J. Exp. Med.* 213:1921–1936. https://doi.org/10.1084/jem.20160670

JEM

Supplemental material

Provided online are four tables. Table S1 lists sequencing details for all HiC samples, showing numbers of sequenced reads, numbers and percentages of paired mappable reads, and numbers and percentages of HiC contact reads. Table S2 lists sequencing details for all Adaptive Immunosequencing samples, showing numbers of total unique complete *Tcrb* rearrangements, numbers of unique *Trbv1* rearrangements, and percentages of *Tcrb* rearrangements involving *Trbv1*. Table S3 lists all oligo sequences for generation of genotyping of mouse lines, as well as qPCR. Table S4 lists all antibodies used for the indicated experiment.